

One year of AU Mic with HARPS - II. Stellar activity and star-planet interaction

Baptiste Klein, Norbert Zicher, Robert D. Kavanagh, Louise D. Nielsen, Suzanne Aigrain, Aline A. Vidotto, Oscar Barragán, Antoine Strugarek, Belinda Nicholson, Jean-François Donati, et al.

▶ **To cite this version:**

Baptiste Klein, Norbert Zicher, Robert D. Kavanagh, Louise D. Nielsen, Suzanne Aigrain, et al.. One year of AU Mic with HARPS - II. Stellar activity and star-planet interaction. Monthly Notices of the Royal Astronomical Society, 2022, 512, pp.5067-5084. 10.1093/mnras/stac761 . insu-03672014

HAL Id: insu-03672014
https://insu.hal.science/insu-03672014

Submitted on 19 May 2022

HAL is a multi-disciplinary open access archive for the deposit and dissemination of scientific research documents, whether they are published or not. The documents may come from teaching and research institutions in France or abroad, or from public or private research centers.

L'archive ouverte pluridisciplinaire **HAL**, est destinée au dépôt et à la diffusion de documents scientifiques de niveau recherche, publiés ou non, émanant des établissements d'enseignement et de recherche français ou étrangers, des laboratoires publics ou privés.



Distributed under a Creative Commons Attribution 4.0 International License

Monthly Notices
of the
ROYAL ASTRONOMICAL SOCIETY

MNRAS **512,** 5067–5084 (2022)
Advance Access publication 2022 March 22

https://doi.org/10.1093/mnras/stac761

One year of AU Mic with HARPS – II. Stellar activity and star–planet interaction

Baptiste Klein [1]★ Norbert Zicher [1] Robert D. Kavanagh [2] Louise D. Nielsen [1,3] Suzanne Aigrain,[1] Aline A. Vidotto [2] Oscar Barragán,[1] Antoine Strugarek [4] Belinda Nicholson,[1,5] Jean-François Donati [6] and Jérôme Bouvier[7]

[1]*Department of Physics, University of Oxford, OX13RH Oxford, UK*
[2]*Leiden Observatory, Leiden University, PO Box 9513, NL-2300 RA Leiden, the Netherlands*
[3]*European Southern Observatory, Karl-Schwarzschild-Straße 2, D-85748 Garching bei München, Germany*
[4]*AIM, CEA, CNRS, Université Paris-Saclay, Université Paris Diderot, Sorbonne Paris Cité, F-91191 Gif-sur-Yvette, France*
[5]*Centre for Astrophysics, University of Southern Queensland, QLD 4350 Toowoomba, Australia*
[6]*Univ. de Toulouse, CNRS, IRAP, 14 av. Belin, F-31400 Toulouse, France*
[7]*Univ. Grenoble Alpes, CNRS, IPAG, F-38000 Grenoble, France*

Accepted 2022 March 14. Received 2022 March 10; in original form 2022 January 21

ABSTRACT

We present a spectroscopic analysis of a 1-yr intensive monitoring campaign of the 22-Myr old planet-hosting M dwarf AU Mic using the HARPS spectrograph. In a companion paper, we reported detections of the planet radial velocity (RV) signatures of the two close-in transiting planets of the system, with respective semi-amplitudes of 5.8 ± 2.5 and 8.5 ± 2.5 m s^{-1} for AU Mic b and AU Mic c. Here, we perform an independent measurement of the RV semi-amplitude of AU Mic c using Doppler imaging to simultaneously model the activity-induced distortions and the planet-induced shifts in the line profiles. The resulting semi-amplitude of 13.3 ± 4.1 m s^{-1} for AU Mic c reinforces the idea that the planet features a surprisingly large inner density, in tension with current standard models of core accretion. Our brightness maps feature significantly higher spot coverage and lower level of differential rotation than the brightness maps obtained in late 2019 with the SPIRou spectropolarimeter, suggesting that the stellar magnetic activity has evolved dramatically over a ∼1-yr time span. Additionally, we report a 3σ detection of a modulation at 8.33 ± 0.04 d of the He I D3 (5875.62 Å) emission flux, close to the 8.46-d orbital period of AU Mic b. The power of this emission (a few 10^{17} W) is consistent with 3D magnetohydrodynamical simulations of the interaction between stellar wind and the close-in planet if the latter hosts a magnetic field of ∼10 G. Spectropolarimetric observations of the star are needed to firmly elucidate the origin of the observed chromospheric variability.

Key words: planet and satellites: formation – stars: activity – stars: imaging – stars: individual: AU Microscopii.

1 INTRODUCTION

Studying the processes driving planet formation and evolution is a key to understand the large diversity in the distribution of exoplanets observed so far (Raymond & Morbidelli 2020). This motivates efforts to detect and characterize planets around pre-main-sequence (PMS) stars. Close-in transiting planets are key targets in this venture. Their bulk density, accessible by measuring both the planet masses, by monitoring the radial velocity (RV) of their host star, and radii, by measuring the depth of their photometric transit curve, is a critical parameter to refine planet formation and evolution models (e.g. Mordasini et al. 2012; Owen & Wu 2017). On the other hand, their atmospheric composition, accessible via transmission spectroscopy, and orbital parameters (e.g. orbit eccentricity and spin-orbit angle) enclose crucial information about their formation (see the reviews of Baruteau et al. 2016; Madhusudhan 2019). Finally, signatures of star–planet interactions such as anomalous stellar activity and flares can, in principle, yield constraints on the planet magnetic properties (Cuntz, Saar & Musielak 2000; Saar & Cuntz 2001; Fischer & Saur 2019).

PMS stars are faint in the optical, and exhibit intense magnetic activity whose manifestations, such as large spots or frequent flares, induce photometric and RV signals which hamper the search for close-in planets around them (e.g. Bouvier & Bertout 1989; Berdyugina 2005; Crockett et al. 2012). As a consequence, only a handful young (< 100 Myr) close-in planetary systems have been revealed so far: most of them are transiting planets detected by the *K2* and *TESS* space missions (David et al. 2016, 2019; Mann et al. 2016b, a; Plavchan et al. 2020; Rizzuto et al. 2020; Mann et al. 2021), and the remainder are non-transiting planets unveiled from the RV wobbles of their host star (Donati et al. 2016; Yu et al. 2017). So far, only two systems younger than 100 Myr, namely AU Mic and V1298 Tau, have planets with well-constrained mean bulk density measured (Cale et al. 2021; Klein et al. 2021; Suárez Mascareño et al. 2021).

★ E-mail: baptiste.klein@physics.ox.ac.uk

© The Author(s) 2022.
Published by Oxford University Press on behalf of Royal Astronomical Society. This is an Open Access article distributed under the terms of the Creative Commons Attribution License (http://creativecommons.org/licenses/by/4.0/), which permits unrestricted reuse, distribution, and reproduction in any medium, provided the original work is properly cited.

Downloaded from https://academic.oup.com/mnras/article/512/4/5067/6552137 by guest on 19 May 2022

Located in the 22-Myr β Pic moving group (Malo et al. 2014; Mamajek & Bell 2014; Messina et al. 2016), AU Microscopii (AU Mic, GJ 803) is the second closest PMS star (D = 9.7248 pc; Gaia Collaboration 2018). This system has been intensively monitored over the past 50 yr for its intense magnetic activity notably inducing $\sim$0.1-mag quasi-periodic photometric variations (e.g. Torres & Ferraz Mello 1973; Rodono et al. 1986; Plavchan et al. 2020; Martioli et al. 2021), and frequent flaring events of variable intensity (e.g. Robinson et al. 2001; Hebb et al. 2007; MacGregor, Osten & Hughes 2020; Martioli et al. 2021). The detection of two transiting Neptune-sized planets from Spitzer and TESS light curves (TESS sectors 1 and 27; Plavchan et al. 2020; Martioli et al. 2021) has increased the already high interest of the scientific community in the system which has been intensively monitored with various state-of-the-art spectrometers since then. These follow-up observations made it possible to measure a zero-compatible spin-orbit angle (Addison et al. 2020; Hirano et al. 2020; Martioli et al. 2020; Palle et al. 2020), and a bulk density of 1.32 ± 0.2 g cm^{-3} for the close-in planet AU Mic b (Cale et al. 2021; Klein et al. 2021). Additionally, a 5σ-upper limit of 20.13 $M_\oplus$ has been reported for AU Mic c in Cale et al. (2021).

We observed the AU Mic system intensively with HARPS over a 10-month period, with the aim of precisely capturing the RV signals induced by the stellar magnetic activity in order to better remove it and detect the two transiting planets (Zicher et al. 2022, hereafter paper I). From a total of 82 observations, we reported 2.4 and 3.4σ detections of AU Mic b and AU Mic c, with estimated masses of $11.7^{+5.0}_{-4.9}$ and $22.2^{+6.7}_{-6.6}$ $M_\oplus$, respectively. These masses significantly differ from the most recent estimates of Cale et al. (2021, 20.1 ± 1.6 $M_\oplus$ and 5σ-upper limit of 20.13 $M_\oplus$ for the masses of AU Mic b and c, respectively), and appear in tension with standard core-accretion models where planet c, about twice as massive as planet b, seems to have accreted less H/He material than the latter (see section 4.5 of paper I).

In the present study, we analyse the magnetic activity of AU Mic from the HARPS spectra published in paper I. The intense magnetic field of the star and the small orbital distances of the transiting planets make this system an excellent candidate to search for planet-induced chromospheric emissions (Strugarek et al. 2019, 2022). The HARPS spectral range allows us to access numerous chromospheric emission lines and search for potential modulations that could be explained by star–planet interactions (Cuntz et al. 2000; Saar & Cuntz 2001; Fares et al. 2010; Cauley et al. 2019; Strugarek et al. 2019). On the other hand, the dense sampling of the stellar rotation cycle makes this data set ideally suited to constrain the brightness distribution at the stellar surface using Doppler imaging (DI), while searching for planet-induced signatures shifting the line profiles (see Petit et al. 2015; Donati et al. 2016; Yu et al. 2017; Klein et al. 2021). After describing the observations and data reduction in Section 2, we investigate the chromospheric activity of the star and search for potential planet-induced modulations in Section 3. In Section 4, we use DI to invert the time-series of HARPS cross-correlation functions (CCFs) while simultaneously searching for the RV signatures of the two close-in planets. We finally conclude, in Section 5, by comparing our results to the literature and presenting future prospects for the system.

2 OBSERVATIONS AND DATA REDUCTION

AU Mic was observed between November 2020 and September 2021 (ESO Periods 106 & 107) with the high-accuracy radial velocity planet searcher (HARPS; Mayor et al. 2003), mounted at the ESO's 3.6-m telescope at La Silla observatory.[1] A total of 91 high-resolution spectra ($\mathcal{R} = 115\,000$) were collected in high-accuracy mode: 22 between 2020 November 15 and December 9, and 69 between 2021 May 24 and September 22. The three observations collected on 2021 August 23, which exhibit strong contamination by the Moon (illumination larger than 99 per cent), along with degraded seeing with full width at half maximum (FWHM) larger than 4 arcsec, are discarded in the following analysis. The remaining observations were taken in good seeing conditions with FWHM of ranging between 0.6 and 2.3 arcsec with a median value of 1.1 arcsec and with an airmass systematially lower than 2. The full journal of observations is given in Table A1.

The data were reduced using version 3.8 of HARPS data reduction software (DRS). The reduced spectra feature signal-to-noise ratios (S/N) per pixel at 550 nm ranging from 45 to 139 with a median value of 102. DRS RVs were derived from densely sampled CCFs with a velocity bin of 0.25 km s^{-1} and feature a dispersion 121 m s^{-1} RMS with median uncertainties of 5.2 m s^{-1} RMS. Two indicators of the line shape, namely the FWHM and bisector inverse slope (BIS; Queloz et al. 2001), were also provided by the DRS (see the detailed description of the RV extraction in the section 2 of paper I).

For the DI inversion process (Section 4), we compute CCFs of 0.85 km s^{-1} velocity bin (corresponding to the velocity bin of HARPS spectra) for each observation using a M2 line mask optimized for the HARPS spectral range (Bonfils et al. 2013). Each CCF was truncated outside of a $\pm$11 km s^{-1} window from the line centre, and residual slopes in the continuum were corrected using a linear fit to the extreme profile wings. As a sanity check, we manually computed the RVs and FWHMs respectively from the first- and second-order moments of the normalized profiles. The resulting time-series differ by no more than $\sim$5 m s^{-1} RMS from their DRS counterparts, confirming that the normalization process has no more than a marginal impact on the centroid of the CCFs for AU Mic.

In what follows, we define the stellar rotational phase using the stellar rotation period $P_{rot} = 4.86$ d reported in Plavchan et al. (2020) and the reference date corresponding to the mid-transit time of AU Mic b (BJD = 2458651.993) also used in the spectropolarimetric study carried out in Klein et al. (2021). All the system parameters used in this study are listed in Table 1.

3 ACTIVITY INDICATORS

In this section, we investigate the non-radiative chromospheric emission of AU Mic from our time-series of HARPS spectra. Optical chromospheric lines are indeed well-known indicators of the surface distribution of the small-scale magnetic field for low-mass stars and correlate generally well with stellar activity RV signals (Bonfils et al. 2007; Boisse et al. 2009; Gomes da Silva et al. 2011). In addition, these lines are the best benchmarks for identifying which of our observations are affected by stellar flares in the absence of simultaneous high-cadence photometric monitoring. Finally, the non-radiative chromospheric emission flux is expected to be one of the best proxies of star–planet interactions (e.g. Saar & Cuntz 2001; Fares et al. 2010; Cauley et al. 2018; Strugarek et al. 2019; Cauley et al. 2019).

[1]Observing programs 105.20N0.001 (PI: Zicher) and 106.21MA.001 (PI: Aigrain)

Downloaded from https://academic.oup.com/mnras/article/512/4/5067/6552137 by guest on 19 May 2022

Table 1. Stellar and planet properties of the AU Mic system used in this study. When taken from the literature, the reference of each parameter value is indicated in the right-hand column†. Note that DI reconstructions are performed assuming a stellar inclination of $i_{DI} = 80°$ (see Section 3). Mid-transit times are given in TBJD – 2457 000 units.

Quantity	Parameter	Value	Reference
Stellar parameters			
Distance	D	9.7248 ± 0.0046 pc	G18
Effective temperature	$T_{\rm eff}$	3700 ± 50 K	A19
Surface gravity	$\log g$	4.39 ± 0.03	From R_S and M_S
Stellar radius	R_S	0.75 ± 0.03 $R_\odot$	W19
Stellar mass	M_S	0.50 ± 0.03 $M_\odot$	P20
Luminosity	L_S	0.09 ± 0.02 $L_\odot$	P09
Age	–	22 ± 3 Myr	M14
Rotation period	$P_{\rm rot}$	$4.8571^{+0.0037}_{-0.0027}$ d	paper I
Projected rotational velocity	$v \sin i_{\rm rot}$	7.8 ± 0.3 km s^{-1}	Kl21
Planet b			
Orbital period	$P_{\rm orb,\,b}$	$8.463\,000 \pm 0.000\,002$ d	M21
Semi-major axis	$a_{\rm p,\,b}$	0.0645 ± 0.0013 au	M21
Mid-transit time	$T_{0,\rm b}$	1330.39051 ± 0.00015 d [BJD]	M21
Planet radius	$R_{\rm p,\,b}$	4.07 ± 0.17 $R_\oplus$	M21
Velocity semi-amplitude	$K_{\rm p,\,b}$	5.8 ± 2.5 m s^{-1}	paper I
Planet mass	$M_{\rm p,\,b}$	11.7 ± 5.0 $M_\odot$	paper I
Bulk density	$\rho_{\rm p,\,b}$	0.97 ± 0.43 g cm^{-3}	paper I
Planet c			
Orbital period	$P_{\rm orb,\,c}$	$18.859\,019 \pm 0.000\,016$ d	M21
Semi-major axis	$a_{\rm p,\,c}$	0.1101 ± 0.0022 au	M21
Mid-transit time	$T_{0,\rm c}$	1342.2223 ± 0.0005 d [BJD]	M21
Planet radius	$R_{\rm p,\,c}$	3.24 ± 0.16 $R_\oplus$	M21
Velocity semi-amplitude	$K_{\rm p,\,c}$	8.5 ± 2.5 m s^{-1}	paper I
Planet mass	$M_{\rm p,\,c}$	22.2 ± 6.7 $M_\odot$	paper I
Bulk density	$\rho_{\rm p,\,c}$	3.66 ± 1.28 g cm^{-3}	paper I

† To gain some space in the table, we use aliases for the references. G18, A19, W19, P20, P09, M14, paper I, Kl21, and M21 stand, respectively for Gaia Collaboration (2018), Afram & Berdyugina (2019), White et al. (2019), Plavchan et al. (2020), Plavchan et al. (2009), Mamajek & Bell (2014), Zicher et al. (2022), Klein et al. (2021), and Martioli et al. (2021).

3.1 Chromospheric emission indices

We compute indices based on the flux in the core of Ca II H & K (3968.47 & 3933.66 Å respectively, hereafter $S_{\rm Ca\,II}$), H α (6562.808 Å), H β (4861.363 Å), Na I D1 & D2 (5895.92 & 5889.95 Å, respectively), and He I D3 (5875.62 Å, hereafter He I) chromospheric lines. As expected from the late spectral type and intense magnetic activity of AU Mic, all these lines exhibit a strong emission reversal, variable from one night to the other (see the full-line profiles in Fig. B1). We used the method of Zechmeister et al. (2018) to compute chromospheric emission indices from the blaze-corrected HARPS spectra in the stellar rest frame. In each case, the mean flux within the line core is divided by the average flux between two reference continuum regions on both sides of the line. Except for H β, we used the integration windows defined in Gomes da Silva et al. (2011) for late-type stars, but broadened to account for the Doppler-broadening of the line given the star's projected equatorial velocity. For H β, the flux is measured on a 1.2-Å window, and the continuum is estimated from 5-Å windows cented on 4855 and 4870 Å.

The resulting time-series of chromospheric emission indices are folded to the stellar rotation phase in Fig. 1. For each chromospheric index, we note that the same handful of points appear almost systematically significantly higher than the typical emission flux. These outliers are most likely attributable to flares occurring shortly before or during the visit. In order to identify which epochs are affected by a flaring event, we compute a master chromospheric index, $C_{\rm m}$ by taking the median-normalized sum of all chromospheric emission indices. We then applied a 3σ-clipping process to the $C_{\rm m}$ time-series and flagged six epochs likely affected by a flaring event, which are listed in Table A1 and marked as black crosses in Fig. 1.

3.2 Search for periodicities

As shown in Fig. 1, the chromospheric emission flux exhibits clear temporal variations, consistent from one index to the other, throughout the time span of our observations (see also the line profiles in Fig. B1). However, the chromospheric indices exhibit a significantly weaker modulation with $P_{\rm rot}$ and seem to evolve on much shorter time-scales than the indicators based on the position and shape of the CCFs (e.g. RV, FWHM, or BIS). Such discrepancy is further evidenced by the low correlation observed between each chromospheric index and the RV time-series (see the Pearson correlation coefficients in Table 2 and the correlation plot in Fig. B2). This suggests that, in contrast to CCF-based indicators whose variations are primarily dominated by brightness inhomogeneities at the stellar surface, the fluctuations in the non-radiative chromospheric flux are most likely caused by complex combination of phenomena (e.g. active regions at the stellar surface, nanoflares, interactions with external bodies) of similar intensity.

The Generalized Lomb-Scargle periodograms (GLS; Zechmeister & Kürster 2009) of the RV, FWHM, BIS, $S_{\rm CaII}$, H α, H β, Na I,

Downloaded from https://academic.oup.com/mnras/article/512/4/5067/6552137 by guest on 19 May 2022

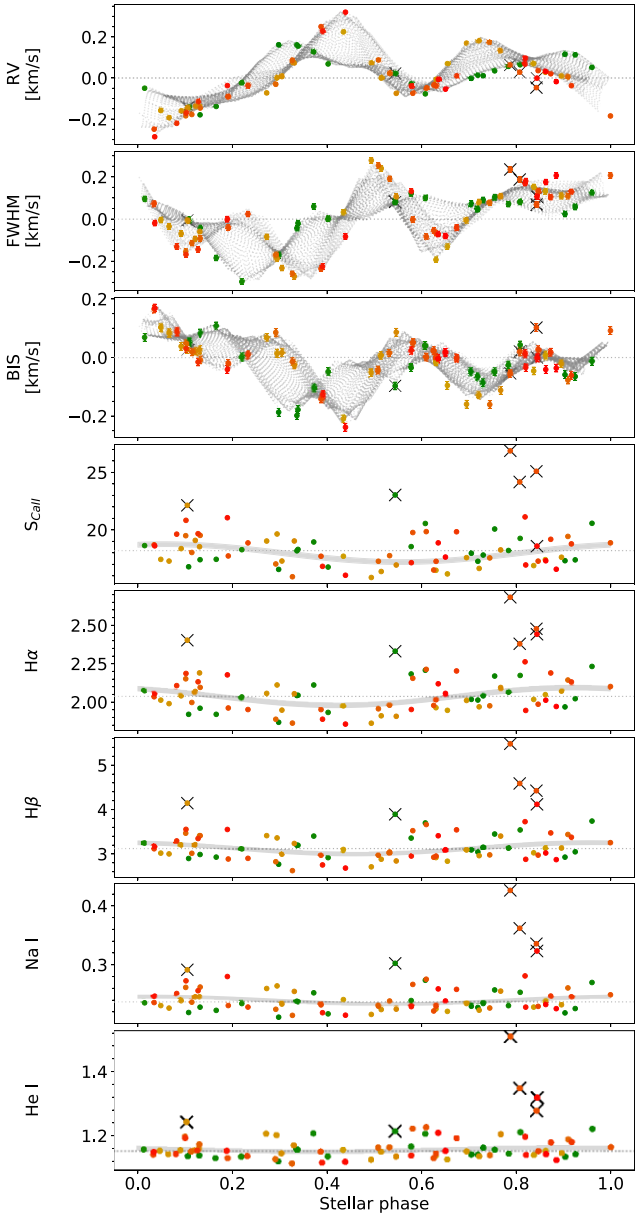


Figure 1. From top to bottom: time-series of DRS-provided RV, FWHM, BIS, and chromospheric emission indicators based on Ca II H & K, Hα, Hβ, Na I, and He I lines, folded at a rotation period of 4.86 d. In each panel, data points of different colours belong to the same stellar rotation cycles (dark green and dark red depict the oldest and most recent observations, respectively). The horizontal dotted lines mark the mean of the data. The grey lines indicate (i) the best-fitting GP prediction in the first three panels (see the description of the fitting procedure in Section 3.2) and (ii) the best-fitting sine-wave (using a least-squares estimator at a period of 4.86 d). Points marked by a black cross were flagged as affected by a stellar flare in Section 3.1.

and He I time-series are shown in Fig. 2. Unsurprisingly, the periodograms of the CCF-based activity indicators exhibit prominent peaks at P_{rot} and its first harmonic. By modelling, each of these time-series independently using a Gaussian Process (GP; Rajpaul et al. 2015) with the quasi-periodic covariance kernel introduced in Haywood et al. (2014) as implemented in the PYANETI python package (Barragán et al. 2022), we find consistent rotation periods of 4.863 ± 0.004 d, 4.86 ± 0.01 d, and 4.867 ± 0.004 d for the RV, FWHM, and BIS time-series, respectively.[2] As illustrated in Fig. 2, we note that including the flares in the GP fit, no more than marginally affects the best-fitting P_{rot}.

The periodogram of each of the chromospheric emission indices exhibits a prominent peak at ∼4.8 d, slightly lower than the photometric stellar rotation period (see Table 2). This suggests that all seven chromospheric emission lines probe similar regions of the stellar atmosphere, and that these regions differ from the main brightness inhomogeneities inducing most of the photometric and CCF variations. We also note that these values lie in between the stellar equatorial and polar rotation periods, respectively equal 4.675 ± 0.006 d and 5.34 ± 0.05 d, measured from the differentially rotating large-scale magnetic field at the surface of AU Mic in Klein et al. (2021). Each chromospheric emission indicator also exhibits a more-or-less prominent peak at a period of 8.33 ± 0.04 d, $\sim 3\sigma$ lower than the orbital period of AU Mic b ($8.463\,000 \pm 0.000\,002$ d). We also note that, for each chromospheric indicator, including the six observations affected by a stellar flare seems to enhance the observed modulation at 8.33 d. However, since (i) the significance of this peak reaches no more than a false alarm probability (FAP) of 10 per cent (for He I), and (ii) other peaks of unclear origin but similar significance are detected at periods of ∼7 and ∼10 d, we caution than this detection remains marginal and that no robust conclusion can be drawn, at this stage, from the chromospheric emission indices alone.

3.3 Bidimensional periodogram analysis

In order to further investigate the putative modulation at 8.33 d unveiled from the chromospheric indices, we compute the bidimensional periodogram of each emission line to quantify the evolution of the flux variability across the line profile, as it is commonly done for young PMS stars (e.g. Johns & Basri 1995; Bouvier et al. 2007; Finociety et al. 2021; Sousa et al. 2021). We first normalize the continuum of each chromospheric line from the blaze-subtracted HARPS spectra in the stellar rest frame. For each spectrum, we mask the chromospheric emission line, as well as all absorption features with relative depth larger than 5 per cent in a 3-nm wide window centred on the chromospheric line. Within the window, we iteratively smooth the spectrum using a Savitzky–Golay filter, reject points deviating by more than 3σ from the mean of the residuals, and repeat the process until no more outlier is flagged. Finally, we interpolate the resulting smoothed spectrum using a cubic spline kernel, and divide the full spectrum within the window by the interpolated function. As a final step, we divide each continuum-normalized spectrum by the median out-of-flare spectrum and compute a GLS periodogram for each velocity bin of the resulting time-series of line profiles using the ASTROPY package (Astropy Collaboration 2013, 2018).

The resulting bidimensional periodograms are shown in Fig. 3, for He I, and in Fig. B3 (respectively Fig. B4) for the other lines with (respectively without) including the observations affected by stellar flares in the input data. We find that the bidimensional periodogram of the He I line exhibits a clear significant peak at a period of 8.33 ± 0.04 d, well-centred on the line profile, present whether we include the flares in the input data set or not. To estimate the significance of the peak, we integrate each normalized line profile over a 16-km s^{-1} wide window centred on the emission line, i.e. where the modulation

[2]Note that the exploration of the parameter space was performed using the method described in section 3.4 of paper I, i.e. by through a Markov chain Monte Carlo sampler in the Bayesian framework.

Downloaded from https://academic.oup.com/mnras/article/512/4/5067/6552137 by guest on 19 May 2022

Table 2. Main results of the analysis AU Mic's chromospheric emission. In lines 1 and 2, we give the best-fitting stellar rotation period for the chromospheric indices and the Pearson correlation coefficient with the RV time-series. In lines 3, we list the best-fitting period at ∼8.3 d (i.e. near the orbital period of AU Mic b) with the associated FAP level. Finally, we give the emitted power associated to this period with and without including the flare-flagged observations (see Section 5.1) in lines 4 and 5.

Chromospheric line	Ca II	H α	H β	Na I	He I
P_{rot}	4.81 ± 0.01 d	4.80 ± 0.01 d	4.80 ± 0.01 d	4.81 ± 0.01 d	4.79 ± 0.01 d
Correlation coef. w/ RV	−0.336	−0.245	−0.258	−0.297	−0.145
$P_{orb,\,b}$	–	–	–	8.35 ± 0.04 d (1 per cent)	8.33 ± 0.04 d (0.2 per cent)
Power (w/ flares)	–	–	–	$9.7 \pm 2.2 \times 10^{17}$ W	$5.4 \pm 1.3 \times 10^{17}$ W
Power (w/o flares)	–	–	–	$5.7 \pm 1.7 \times 10^{17}$ W	$2.9 \pm 0.9 \times 10^{17}$ W

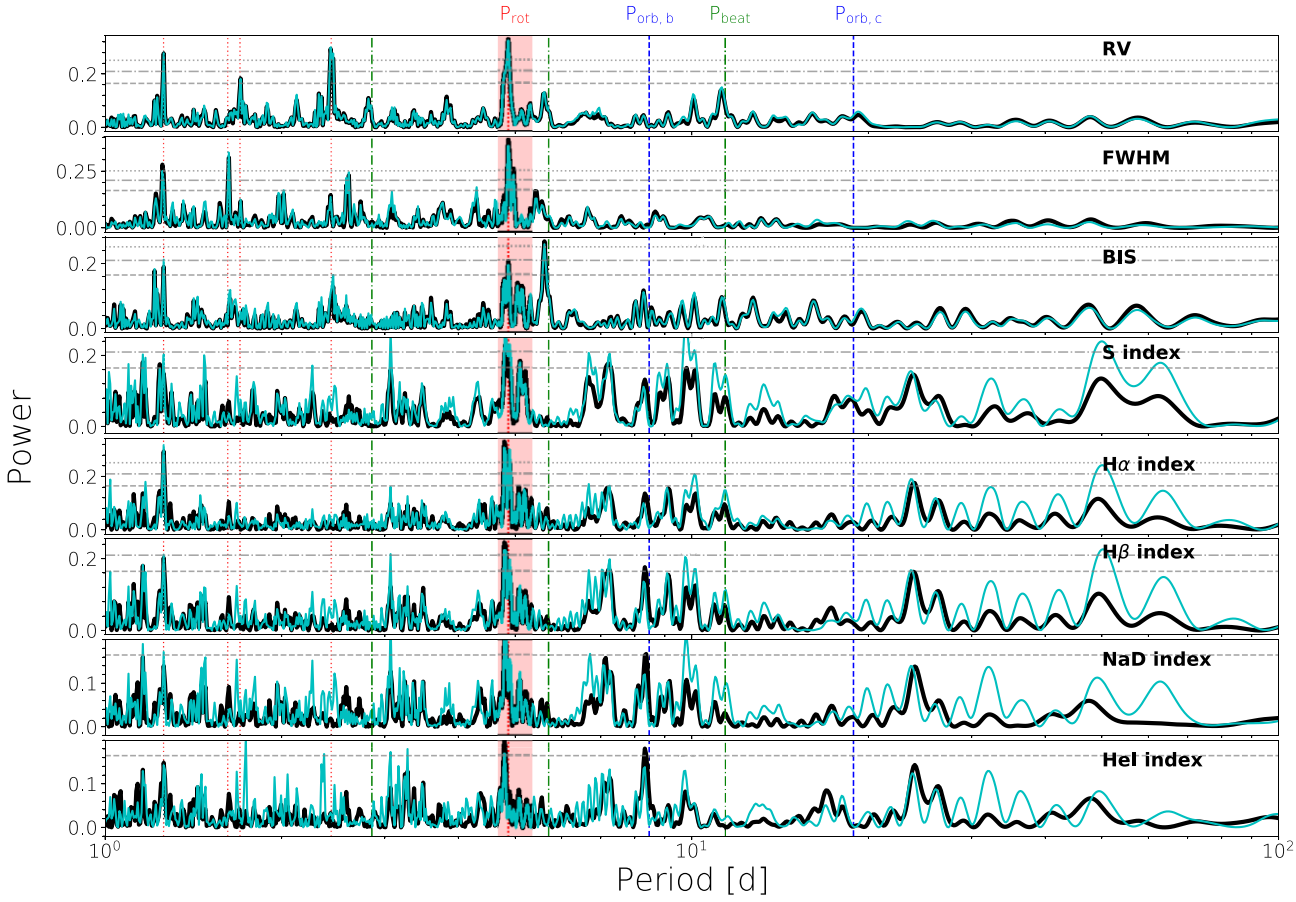


Figure 2. From top to bottom: GLS periodograms of the time-series of RVs, FWHMs, BISs, and chromospheric emission indicators based on Ca II H & K, H α, H β, Na I, and He I lines. In each panel, the thick black and thin cyan solid lines, respectively, show the GLS periodograms of the full data set and of the data set after excluding the observations affected by flares flagged in Section 3.1. The horizontal dashed, dash–dotted and dotted grey lines indicate the false alarm probabilities of respectively 10, 1, and 0.1 per cent, computed using the method of Baluev (2008). The red vertical dotted lines indicate the stellar rotation period and its harmonics, i.e. from left to right, $1 - f_{rot}$, $3f_{rot}$, $1 - 2f_{rot}$, $2f_{rot}$, and f_{rot}, where $f_{rot} = 1/P_{rot}$. The red vertical band delimits the equatorial and polar rotation periods (4.675 ± 0.006 d and 5.34 ± 0.05 d, respectively) measured for the large-scale magnetic field of AU Mic in Klein et al. (2021). The orbital periods of planets b and c are marked by the blue vertical dashed lines. Finally, the green vertical dash–dotted lines indicate the the beat period (P_{beat}) between AU Mic b and its host star, as well as its second and fourth harmonics (see Section 5.1 and Fig. 9). Note that the spectral window of the observations, shown in the fig. 3 of paper I, does not exhibit any significant peak at the periods of interest. Note also that the periodograms were computed using the ASTROPY PYTHON module (Astropy Collaboration 2013, 2018).

is strongest, and compute the GLS periodogram of the resulting time-series. Using a bootstrap-based method to estimate the FAP levels, we find that the peak at 8.33 d reaches FAP levels of 0.2 per cent and 1 per cent when the flares are respectively included and excluded from the data set. As a sanity check, we built 100 data sets by removing a third of the data points randomly chosen within the observational dates and found that the peak was systematically detected at a confidence larger than 2σ, reinforcing the non-spurious nature of this detection. As a final test, we created two subsets, C_1 and C_2, of data from the time-series of continuum-normalized He I profiles, containing the data collected at planet orbital phases[3] respectively

[3]The orbital phase of AU Mic b is defined using the planet mid-transit time given in Section 2 (i.e. BJD = 2458651.993) and the planet orbital period given in Table 1 (i.e. 8.463 d).

Downloaded from https://academic.oup.com/mnras/article/512/4/5067/6552137 by guest on 19 May 2022

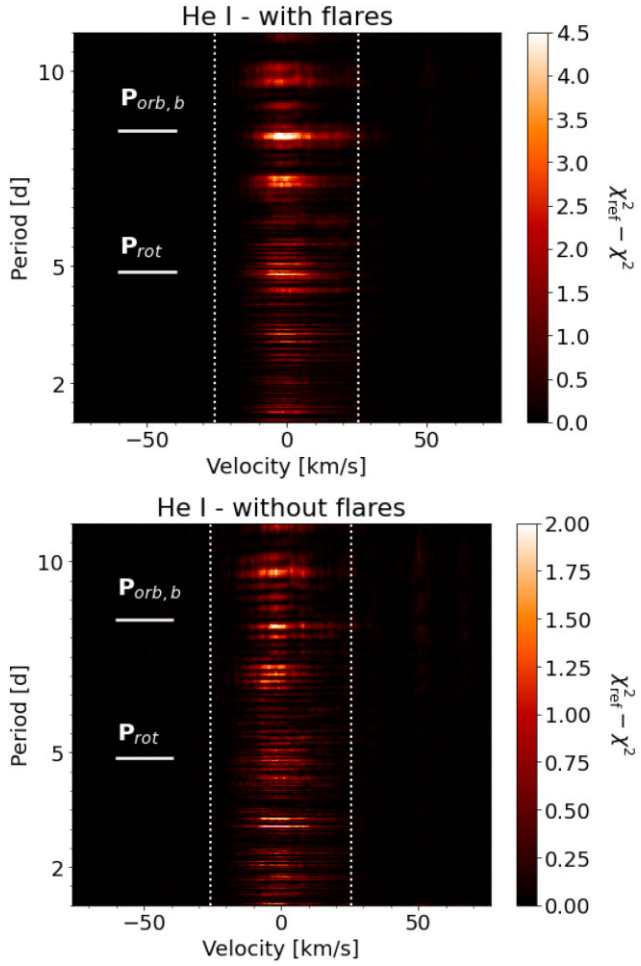


Figure 3. 2D periodograms for the He I D3 line (5875.62 Å). Each vertical line is a GLS periodogram computed with the ASTROPY PYTHON module (Astropy Collaboration 2013, 2018). For each column, the colour code depicts the difference in reduced-χ^2 of the residuals between the best-fitting constant reference model, $\chi^2_{\rm ref}$, and the best-fitting simple sine-wave model for each period on the Y-axis, χ^2. The two white vertical-dotted lines mark the blue- and red-hand sides of the line core.

between 0.75 and 0.25 (when the planet is closer from the observer than the star) and between 0.25 and 0.75 (i.e. when the star is closer from the observer than the planet). The bidimensional periodograms of C_1 and C_2 are shown in Fig. B5. We find that the peak at 8.33 d almost completely disappears in case C_2, whereas the signal is still clearly identified (even though noisier) in case C_1, which corresponds to what one would have expected if the observed modulation is indeed due to a planet-induced hotspot in the stellar atmosphere. We however caution that, since the selected subsets C_1 and C_2 are based on the planet orbital period, the search for peaks around a 8.33-d period in each of these subsets incurs the risk of aliasing, and that no firm conclusion can be drawn from this analysis alone.

As shown in Fig. B3 and B4, a prominent peak at 8.33 d is similarly identified from the Na I lines but the latter is only tentatively detected when the observations affected by stellar flares are excluded from the data set. This modulation remains no more than marginally detected from the Hα and Hβ line profiles, whose bidimensional periodograms are dominated by the stellar rotational modulation. Similarly, no detection can be claimed from the Ca H & K lines which, as expected from Fig. 2, exhibit chaotic bidimensional periodograms with multiple peaks between 7 and 10 d of unclear origin. While the late spectral type of AU Mic means that the continuum SNR is relatively low at the around the Ca H & K lines, it is not clear that this alone explains the apparently noiser periodogram for those lines. The continuum-normalized emission flux within the Ca H & K lines does not exhibit any correlation with the airmass or the SNR of the observations, which would have been expected if the lines were affected by atmospheric dispersion or low-signal noise.

4 BRIGHTNESS IMAGING

4.1 Description of the method

In this section, we propose to jointly recover both the stellar brightness topologies and the planet orbital parameters from the time-series of HARPS CCFs using DI (e.g. Vogt, Penrod & Hatzes 1987; Semel 1989; Brown et al. 1991; Donati & Brown 1997; Donati et al. 2000, 2014). Our DI code models the stellar surface as a dense grid of 5000 cells, each featuring a relative brightness coefficient (resp. 1, >1, and <1 for the quiet photosphere, bright plage, and dark spot). At each observation date, local intensity line profiles are computed for each cell in the visible hemisphere of the star using Unno-Rachkovsky's analytical solution to the radiative transfer equations in a Milne–Eddington atmosphere (Unno 1956). These local line profiles are then (i) Doppler-shifted according to the local RV of the cell, (ii) weighted by the local limb-darkening, sky-projected area and local brightness, and (iii) combined into global line profiles and compared to the observed CCFs. In practice, we use a conjugate gradient algorithm to iteratively compute brightness topologies until the time-series of synthetic line profiles matches the observed CCFs down to a user-provided χ^2. The degeneracy of the inversion problem is overcome by imposing a maximum-entropy regularization condition following Skilling & Bryan (1984), i.e. by choosing the brightness distribution with the minimum spot coverage.

In moderately fast rotators like AU Mic, the unknown intrinsic profile of the star still significantly contributes to the width and depth of the observed line profiles. In order to ensure that the DI code focuses on reconstructing activity-induced profile distortions rather than systematic differences between synthetic and observed line profiles (see Hébrard et al. 2016), we use the iterative procedure described in Klein et al. (2021). We first use our DI code to perform a maximum-entropy inversion of the observed line profiles $\boldsymbol{I}_{\rm obs}$, which provides a time-series of synthetic profiles $\boldsymbol{I}_{\rm syn}$. We then subtract the median difference between $\boldsymbol{I}_{\rm obs}$ and $\boldsymbol{I}_{\rm syn}$ from $\boldsymbol{I}_{\rm obs}$ and repeat the process until the median difference between $\boldsymbol{I}_{\rm obs}$ and $\boldsymbol{I}_{\rm syn}$ is flat (which takes typically 5–10 iterations). Similarly to Klein et al. (2021), we find that this procedure marginally affects the profile RVs for AU Mic. This is due to the fact that both stellar rotation and close-in planet orbital periods are significantly lower than the total time span of the data. As a consequence, both profile distortions (due to stellar activity) and shifts (mostly due to the close-in planets) are averaged out in the median difference between $\boldsymbol{I}_{\rm obs}$ and $\boldsymbol{I}_{\rm syn}$.

We then adapt the method introduced in Petit et al. (2015) and applied in e.g. Donati et al. (2017), Yu et al. (2017), Klein et al. (2021), and Heitzmann et al. (2021). We simultaneously search for planet-induced shifts in AU Mic's CCF time-series whilst correcting for their activity-induced distortions using DI. Consistently with the transit analyses, we model each planetary RV signal, $V_{\rm p}$, assuming that the planet orbits are circular, such that

$$V_{\rm p}(t) = K_{\rm p} \sin\left[2\pi \frac{T_0 - t}{P_{\rm orb}}\right], \quad (1)$$

Downloaded from https://academic.oup.com/mnras/article/512/4/5067/6552137 by guest on 19 May 2022

where K_p is the semi-amplitude of the planet RV signature, and T_0 and P_{orb} are the planet mid-transit time and orbital period. In the fiducial case, we assume that AU Mic b and AU Mic c are perfectly phased with their respective transit curves, leaving their velocimetric semi-amplitudes as the only free planet parameters. Our DI code includes a solar-like model of differential rotation (DR) as described in Donati et al. (2000) and Petit, Donati & Collier Cameron (2002). The evolution of stellar rotation rate Ω as a function of the colatitude θ is described by

$$\Omega(\theta) = \Omega_{eq} - d\Omega \cos^2 \theta, \quad (2)$$

where Ω_{eq} is the rotation rate at the stellar equator and $d\Omega$ is the difference of rotation rate between the stellar equator and the pole. We carry out the inversion of the observed CCFs for a wide range of planet and DR parameters. For each set of parameters, the line profiles are shifted according to the planet RV signature given by equation (1) and then reconstructed with DI up to a given level of entropy (i.e. spot coverage), thus yielding a value of χ^2 quantifying the goodness of DI fit. The best parameters and their error bars are estimated afterwards from the χ^2 map using Press et al. (1992)'s statistics.

4.2 Application to AU Mic

Intrinsic stellar variability is not yet included in the current version of our DI code. We thus divide our time-series of HARPS CCFs into two subsets of data, $\boldsymbol{I_{2020}}$ and $\boldsymbol{I_{2021}}$, containing respectively the 21 observations taken in November/December 2020 and the remaining 61 observations collected in 2021, after removing Moon- and flare-contaminated line profiles. We then perform the DI analysis independently on each data set. These two subsets of data respectively span 24 and 121 d (i.e. respetively 5 and 25 stellar rotation cycles), lower or of similar length to the ∼100-d time-scale on which AU Mic's activity signal evolves (Plavchan et al. 2020). In each DI reconstruction, we adopt a linear limb-darkening law of coefficient 0.66 (Claret & Bloemen 2011), an axial inclination of $i_{DI} = 80°$,[4] and a $v \sin i_{rot}$ of 7.8 km s^{-1} (see Weise et al. 2010; Klein et al. 2021).

We apply the process described in Section 4.1 to independently invert $\boldsymbol{I_{2020}}$ and $\boldsymbol{I_{2021}}$ into surface brightness topologies and planet velocimetric semi-amplitudes. We find that the 2020 data set is consistent with a solid-body rotation at a rotation period of 4.85 ± 0.01 d, in line with the photometric rotation period 4.86 d (see Table 1). In a similar way, the 2021 profiles are found to be sheared by a weak DR with $\Omega_{eq} = 1.294 \pm 0.001$ rad d^{-1} and $d\Omega = 0.013 \pm 0.005$ rad d^{-1}, implying rotation periods of 4.856 ± 0.004 and 4.90 ± 0.03 d at the equator and pole, respectively.

The reduced χ^2 maps are shown in the (K_b, K_c) space at the best-fitting DR parameters for both data sets in Fig. 4. Unsurprisingly, the relatively low number of data points on the 2020 period (21 profiles of 26 data points each) makes it impossible to recover any of the two planets from the $\boldsymbol{I_{2020}}$ data set alone. In contrast, we obtain a 3.3-σ detection of a planetary signal of semi-amplitude of $K_c = 13.3 \pm 4.1$ m s^{-1} at the orbital period of AU Mic c, whereas the RV signature of AU Mic b remains no more than marginally recovered, with a semi-amplitude of $K_b = 7.1 \pm 3.8$ m s^{-1}. To ensure that the recovered signals are indeed of planetary origin, we reapplied

[4]Note that, although the axial inclination of AU Mic is likely close to 90°, imposing a stellar inclination of 80° in the DI reconstruction allows one to prevent any north–south degeneracy. Note that, as shown for example in Petit et al. (2015), variations of stellar inclination $\lesssim 10°$ marginally affect the recovered brightness topology and planet orbital parameters.

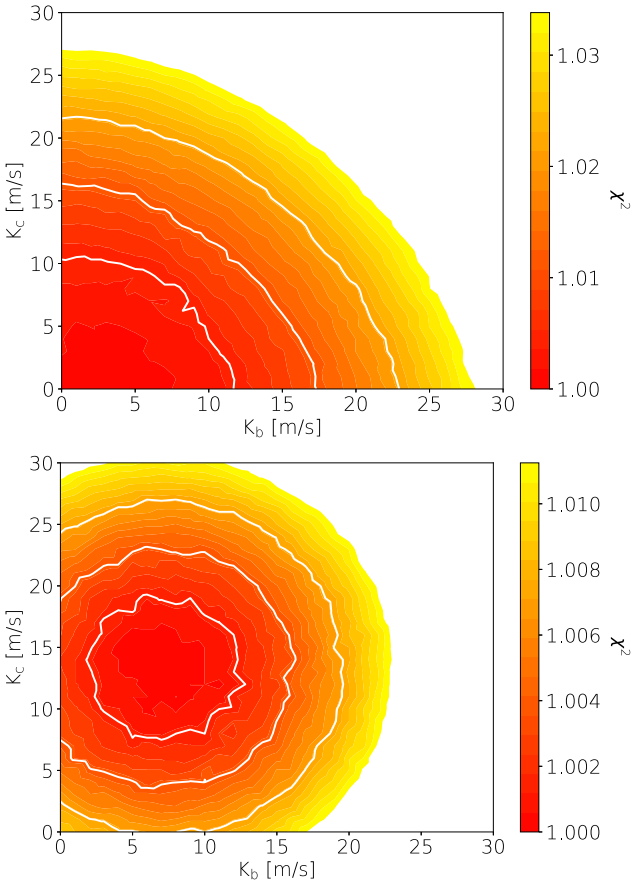


Figure 4. 2D χ^2_r maps obtained by performing brightness reconstructions of the time-series of HARPS CCFs collected over the November-December 2020 period (top panel) and over the May-September 2021 period (bottom panel). The DI reconstructions shown here are performed assuming the best-fitting DR parameters obtained for each period (see Section 4.2). In each panel, the 1, 2, and 3σ levels are depicted by white solid lines.

the DI process to the 2021 data set but, this time, freezing the DR parameters to their best estimates and leaving the two orbital periods and velocimetric semi-amplitudes of the planets as free parameters of the model. We recovered orbital periods of 8.47 ± 0.01 and 18.87 ± 0.02 d for AU Mic b and AU Mic c, both fully consistent with the literature values (see Table 1). Moreover, the planet semi-amplitude estimates remain similar, but slightly less precise than their counterparts from the previous paragraph.

The maximum-entropy fits to the HARPS CCFs, shown in Figs 5 and 6 for $\boldsymbol{I_{2020}}$ and $\boldsymbol{I_{2021}}$, respectively, reproduce the observations down to $\chi^2_r = 1$. The corresponding brightness topologies, respectively shown in the top and bottom panel of Fig. 7, feature consistent spot coverages of 4.7 per cent and 5.1 per cent (typical error bar of 0.5 per cent). Both maps exhibit more dark spots than bright plages, all preferentially located near the stellar equator. We note that the reconstructed features appear more spread out in 2021 than 2020, which is most likely attributable to the intrinsic evolution of the magnetic activity throughout the 2021 observations.

We now apply the process described in Section 4.1 to the whole time-series of HARPS CCFs, from November 2020 to September 2021 (82 observations). By doing so, our DI fit relies on more observational constraints and, thus, might yield more precise mass estimates for the two planets, provided that the brightness distribution has not radically changed throughout the observations. We impose a solid-body rotation in the DI reconstruction, to keep consistency with

Downloaded from https://academic.oup.com/mnras/article/512/4/5067/6552137 by guest on 19 May 2022

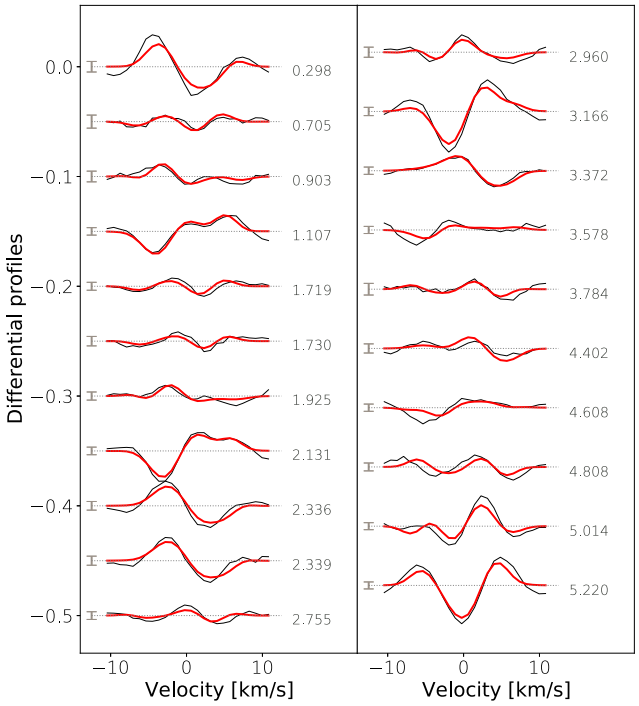


Figure 5. Time-series of observed (black thin lines) and synthetic (red thick lines) mean-subtracted line profiles (a.k.a. differential profiles) collected in 2020. The stellar rotation cycle is written at the right-hand side of each profile whereas the $\pm 1\sigma$ uncertainties on the line continuum is indicated at the left-hand side of the profiles. Note that the stellar rotational cycles are counted from the cycle corresponding to the first observation collected over the 2020 period.

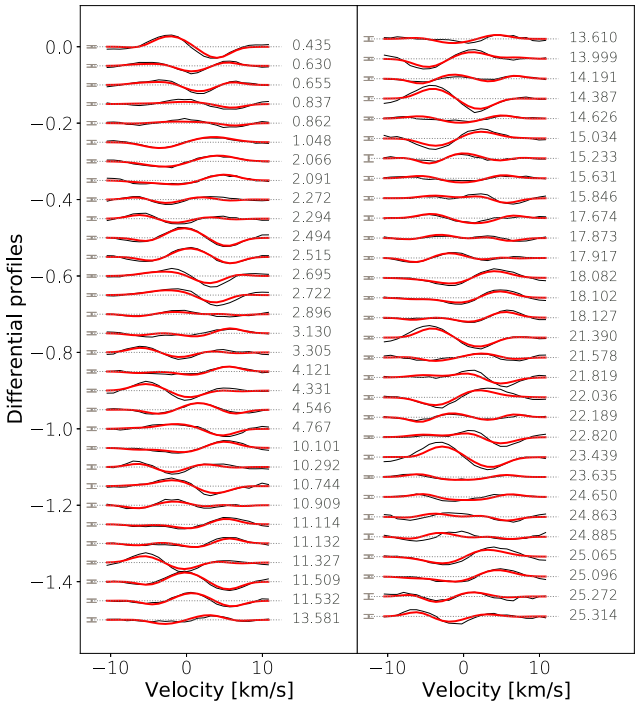


Figure 6. Same as Fig. 5, but, this time, for the observations collected on the 2021 period. Note that the stellar rotational cycles are counted from the cycle corresponding to the first observation collected over the 2021 period.

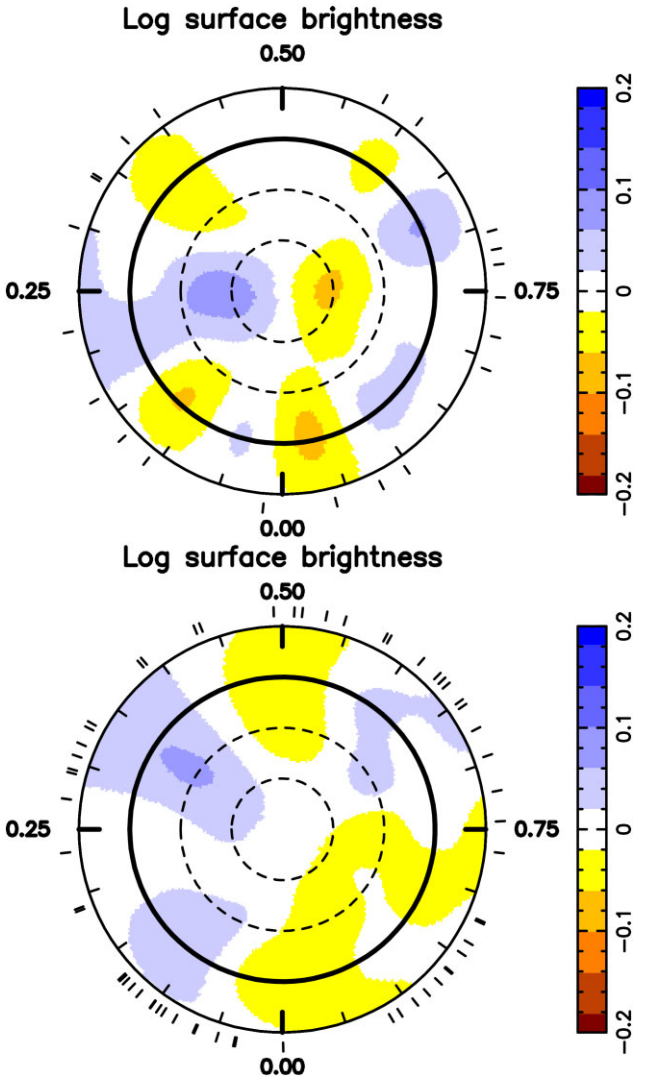


Figure 7. Best-fitting brightness topologies of AU Mic from 2020 (top panel) and 2021 (bottom panel) data sets. Each panel is a flattened polar view of the surface of the star where the colour scale depicts the logarithm of the relative surface brightness. The stellar pole is located at the centre of the plot whereas the concentric circles indicate the stellar equator (solid line) and $-30°$, $30°$, and $60°$ parallels. The radial ticks around the star mark the phases of observations.

the results individually obtained on both data sets. Unsurprisingly, our best DI reconstruction cannot reproduce the observed profile to a reduced χ^2 lower than $\sim$2, which is most likely attributable to the evolution of stellar activity over the last year. We barely recover the velocimetric semi-amplitudes of both planets, confirming that the intrinsic evolution of the stellar activity is the limiting factor on the accuracy of our planet mass estimates.

5 CHROMOSPHERIC ACTIVITY AND STAR–PLANET INTERACTION

In this study, we conducted a spectroscopic analysis of the magnetic activity of AU Mic from an intensive 10-month monitoring campaign with HARPS. In this section, we compare our results to the recent literature and discuss their implications on stellar activity, planet formation and evolution, and star–planet interactions.

Downloaded from https://academic.oup.com/mnras/article/512/4/5067/6552137 by guest on 19 May 2022

5.1 Chromospheric activity and star–planet interactions

CCF-based activity indicators (i.e. RV, FWHM, BIS) show a clear rotational modulation, slowly evolving from November 2020 to September 2021, which echoes the brightness distributions obtained with DI (see Fig. 7). As expected from the young age and late spectral type of AU Mic, each of the Ca II H & K, Hα, Hβ, Na I D1 & D2, and He I D3 chromospheric lines presents a strong time-evolving emission reversal. The non-radiative emission flux in each line appears modulated at a typical period of 4.80 d, 6-σ shorter than the photometric/velocimeter stellar rotation period (4.86 d). This discrepancy is discussed in Section 5.3. We also note that the non-radiative chromospheric flux also exhibits significantly more short-term variability than the CCF-based indicators, suggesting that the observed emission is resulting from a combination of different physical processes.

5.1.1 Origin of the 8.33-d modulation

Each chromospheric emission index exhibits a more-or-less prominent modulation at a period of 8.33 ± 0.04 d, most robustly detected from the bidimensional periodogram of the He I line (FAP of 0.2 per cent). This emission signal could potentially be induced by star-planet magnetic interactions (SPMI) between planets b and/or c and its host star. From the large-scale magnetic topology of the star published in Klein et al. (2021), Kavanagh et al. (2021) have shown that, for a relatively low mass-loss rate of 27 $\dot{M}_\odot$ (Plavchan et al. 2009), planets b and c orbit in the sub-Alfvénic region of the stellar wind.[5] In this configuration, the interaction between the planet and the stellar magnetic field is expected to produce Alfvén waves, which travel from the planet to the star along the field line connecting the two bodies, inducing potentially observable signatures in the stellar atmosphere (e.g. Cuntz et al. 2000; Ip, Kopp & Hu 2004; Fischer & Saur 2019; Strugarek et al. 2019). A sketch of this scenario is shown in Fig. 8.

The power P of the Alfvén waves generated in this interaction is (Saur et al. 2013)

$$P = \pi^{1/2} {R_\mathrm{p}}^2 B \rho^{1/2} \Delta u^2 \sin^2\theta, \tag{3}$$

where R_p is the planet radius, and B and ρ are the stellar wind magnetic field strength and density at the position of the planet, respectively. Δu is the relative velocity between the stellar wind and planetary orbit, and θ is the angle between the vectors $\boldsymbol{B}$ and $\Delta\boldsymbol{u}$. If the observed modulation is induced by the deposition of this energy at the foot point of the field lines connecting one or both planets to the star, one would expect the observed signal to be modulated at the orbital period of the planet (Cuntz et al. 2000; Saar & Cuntz 2001; Strugarek 2018; Fischer & Saur 2019). This theoretical explanation is strengthened by the fact that the observed modulation disappears when the orbital phases of planet b lie between 0.25 and 0.75. However, the systematic 0.13-d difference between the observed modulation period and $P_{\mathrm{orb,\,b}}$ is hard to reconcile with standard SPMI models. As outlined by Fischer & Saur (2019, hereafter F19), in the ideal case of a stellar magnetic dipole nearly aligned with the stellar rotation axis and perpendicular to the planet orbital plane, star–planet interactions are likely to induce observable signatures modulated at the beat period of the system, P_beat, given by

$$P_\mathrm{beat} = \frac{2\pi}{\Omega_\mathrm{star} - \Omega_\mathrm{p}}, \tag{4}$$

[5]Note that he solar mass loss rate $\dot{M}_\odot$ is assumed equal to 2×10^{-14} $\mathrm{M_\odot\ yr^{-1}}$ (Wood et al. 2005).

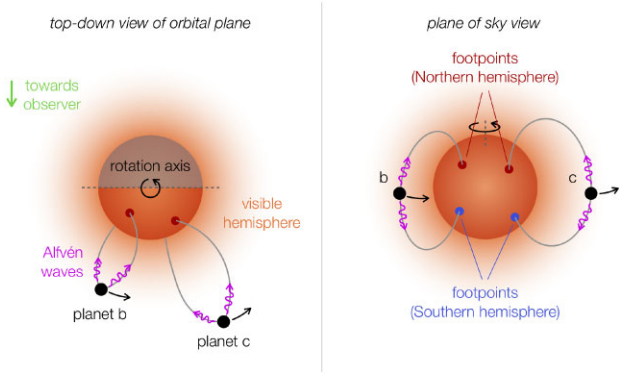


Figure 8. Sketch of the scenario where regions of enhanced emission are induced on the stellar surface of AU Mic via a sub-Alfvénic interaction between the star's magnetic field and the orbiting planets. In a sub-Alfvénic orbit, a planet can produce Alfvén waves that carry energy back towards the stellar surface along the field line connecting to the planet. If the point where the field line connects to the stellar surface (foot point) appears on the hemisphere visible to the observer (left), enhanced chromospheric emission may appear. As planets b and c both orbit in the closed-field region of the star's magnetic field (see Kavanagh et al. 2021), they may each produce up to two visible foot points on the stellar disc (right).

where Ω_star and Ω_p are the respective angular velocities of the star and planet.

This effect can be investigated further using the 3D magneto-hydrodynamical simulations of AU Mic's stellar wind presented in Kavanagh et al. (2021), based on the magnetic topology obtained from the 2019 SPIRou observations of the star (Klein et al. 2021). We use the stellar wind model of AU Mic which predicts that both planets b and c are predominantly in sub-Alfvénic orbits, corresponding to a mass-loss rate of 27 $\dot{M}_\odot$. With this model, we compute the positions of the foot points of the stellar magnetic field lines connecting from planets b and c to the stellar surface, for 500 stellar rotations beginning at the reference time for cycle phase zero of BJD = 2458651.993 (Klein et al. 2021). This provides us with both full temporal coverage of our HARPS observations, and also allows us to assess the long-term evolution of the simulated planet-induced signal. At this reference time, the orbital phases of planets b and c are 0.91 and 0.32, respectively.

Over the 500 rotations of the star, we compute the positions of the foot points of the lines connecting to both planets b and c. If the foot points lie on the hemisphere visible to the observer (as illustrated in the left-hand panel of Fig. 8), we compute the power deposited at the foot point using equation (3). The resulting simulated power induced by the planets is shown in the top panel of Fig. 9. The simulated signals from planets b and c are visible 66 per cent and 46 per cent of the time respectively, with either signal being visible for 81 per cent of the time. The estimated signal has an average strength of 1.6×10^{15} W, and a peak strength of 1.3×10^{16} W. Note here that we explicitly assume that all of the power carried by the Alfvén waves is deposited at the foot points. In reality however, it is likely that only a small fraction of the energy would be converted into enhanced emission in the chromospheric lines.

In the bottom panel of Fig. 9, we show the associated GLS periodogram computed from the simulated planet-induced signal. We find that for the individual simulated signals induced by planets b and c, there is strong periodicity at their respective orbital and beat periods, in line with the estimates of F19. We also see significant periodicity at harmonics of the beat periods, and at the stellar rotation period, albeit to a lesser extent. We note that no such

Downloaded from https://academic.oup.com/mnras/article/512/4/5067/6552137 by guest on 19 May 2022

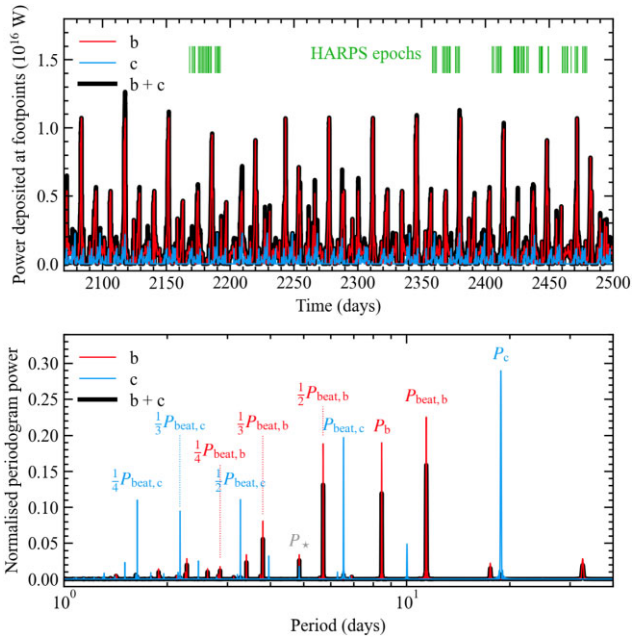


Figure 9. *Top:* power deposited at the foot points of the stellar magnetic field lines connecting to planets b and c during the HARPS observations, computed using the simulated stellar wind environment of AU Mic presented in Kavanagh et al. (2021). The times are given in TBJD − 2457 000. The thin red/blue lines show the individual contribution of planets b and c, respectively, and the thick black line shows the sum of the two signals. Vertical green lines illustrate the epochs of the HARPS observations. *Bottom*: GLS periodograms computed for the simulated planet-induced signal. Again, we show the results for the individual (thin red/blue lines) and sum of the two signals (thick black line). The signals induced by planets b and c show strong periodicity at their respective orbital periods, as well as the fundamental and harmonics of their beat periods (see equation 4). Both also show periodicity at the stellar rotation period, albeit at a lesser extent than at the aforementioned values. For the sum of the two signals, the periodicity mirrors that of the signal induced by planet b, which is roughly an order of magnitude stronger than that induced by planet c due to its close proximity to the star (see top panel).

peak can be firmly identified from the periodograms shown in Fig. 2. In the same way, no modulation at 8.33 d is seen from the computed planet-induced power, which might just reflect the fact that the magnetic topology of AU Mic has significantly evolved since 2019. The respective stellar rotation periods required to obtain $P_{\rm beat} = 8.33$ d for AU Mic b and c are 4.2 and 5.7 d, i.e. inconsistent with the equatorial and polar rotation periods of 4.675 and 5.34 d reported in Klein et al. (2021). Similarly, the peak at 8.33 d does not match the beat period between the two transiting planets nor its first harmonic. As a consequence, the observed 8.33-d modulation, if indeed attributable to a SPMI, is likely a combination of several processes hard to disentangle without simultaneous information on the magnetic topology.

5.1.2 *Comparison to the emitted power of the chromospheric lines*

We now compare the power of the periodic emission lines to that available via sub-Alfvénic interactions with planets b and c. Following the methodology introduced in Strugarek et al. (2019), we assume that the continuum spectrum of the chromospheric lines is locally well-described by a blackbody with $T_{\rm eff} = 3700$ K. The blackbody radiance is integrated over the width of the He I D3 line in our observed spectra, and the result is integrated over all emission angles in order to quantify a flux hypothetically distributed over the whole stellar disc. We then rescale this flux estimate by the relative area of the footprint at the stellar surface, assumed here to be of 0.1 per cent (Strugarek et al. 2019). We finally fit a double sine-wave at respective periods of 4.8 d (to account for stellar-induced emission) and 8.33 d (potential SPMI signature) to the time-series of out-of-flare He I emission flux. We find that the emitted power at 8.33 d features a semi-amplitude of a few 10^{17} W (see Table 2). Similar emitted powers are estimated from the Na I doublet. These values are about one order of magnitude larger than the power estimated from our 3D magnetohydrodynamic simulations (see Fig. 9).

The power of the planet-induced signal may be larger than that shown in the top panel of Fig. 9 if planets b/c possess intrinsic magnetic fields. In this scenario, the radius of the planet in equation (3) is replaced by the size of the planetary magnetosphere (see Kavanagh et al. 2021). The sub-Alfvénic region of the stellar wind is dominated by magnetic forces, so the size of the magnetosphere can be approximated as (Kavanagh et al. 2019)

$$R_{\rm M} = \left(\frac{B_{\rm p}}{B}\right)^{1/3} R_{\rm p}, \tag{5}$$

where $B_{\rm p}$ is the polar magnetic field strength of the planet, and B is the field strength of the stellar wind at the position of the planet. At the orbit of planet b, which induces the majority of the power at the foot points, the magnetic field strength of the stellar wind is on average 0.1 G. Plugging this value in to equation (5), we find a magnetosphere radius of $\sim 5\,R_{\rm p,\,b}$ to explain the observed emitted power of 3×10^{17} W, implying a typical magnetic field of $B_{\rm p} \approx 10$ G, typically one order of magnitude below the strengths of the magnetospheres of hot Jupiters estimated in Cauley et al. (2019).

An additional source of energy may be produced if the sub-Alfvénic star–planet interactions results in the release of energy from coronal loops, as suggested by Lanza (2009). This is thought to occur via the stretching of the foot point on the stellar surface (Lanza 2013; Cauley et al. 2019). The total power available from this interaction is

$$P = \frac{1}{2} f_{\rm p} {R_{\rm p}}^2 {B_{\rm p}}^2 \Delta u \tag{6}$$

where $f_{\rm p}$ is the fraction of the planetary hemisphere covered by flux tubes, which depends on the ratio $B/B_{\rm p}$ (Lanza 2013). Assuming that 0.2 per cent of the total available power is radiated away in He I as estimated by Cauley et al. (2019) based on Ca II H & K lines, we would require a planet magnetic field of 10–20 G to reach the observed power, which is consistent with our estimate from the last paragraph.

We caution that firmly confirming that the observed modulation of the He I flux at 8.33 d is indeed due to a SPMI is a challenging task. First and foremost, the magnetic topology of the star has been demonstrated to be a critical ingredient to hunt for potential signatures of SPMIs. Such information can only be obtained by inverting high-resolution circularly polarized line profiles into a distribution of the large-scale field vector at the stellar surface with Zeeman–Doppler imaging (see the reviews from Donati & Landstreet 2009; Kochukhov 2016). Hence the need to keep on monitoring the system, but, this time, with high-precision spectropolarimetres (e.g. HARPS-Pol, CRIRES+, SPIRou), in order to simultaneously recover the non-radiative chromospheric emission flux on many lines [spanning both the optical and near-infrared (nIR) domains] and the associated magnetic topology. On a final note, we find that including the six epochs affected by flares identified in Section 3.1 tends to increase the significance of the emission flux modulated at 8.33 d. More spectroscopic observations of consecutive flaring events of

Downloaded from https://academic.oup.com/mnras/article/512/4/5067/6552137 by guest on 19 May 2022

AU Mic in different spectral domains (from X-rays to nIR) would greatly help investigating whether some of these flares could be induced by magnetic interactions between the star and its close-in planets, as suggested in Lanza (2018) and F19.

5.2 New mass estimates for AU Mic close-in planets

From our estimates of $K_b = 7.1 \pm 3.8\,m\,s^{-1}$ and $K_c = 13.3 \pm 4.1\,m\,s^{-1}$, we obtain planet masses of $M_b = 14.3 \pm 7.7\,M_\oplus$ and $M_c = 34.9 \pm 10.8\,M_\oplus$. These estimates are slightly larger but still consistent within 1σ with the planet masses obtained in paper I by jointly modelling the stellar activity signals and the planet RV signatures using a multidimensional GP framework (Rajpaul et al. 2015; Barragán et al. 2022). Over the 121 d spanned by our 2021 data set, AU Mic's brightness topology has significantly evolved (see Fig. 6). As this intrinsic evolution is not yet included in our DI code, the corresponding masses are significantly less precise than their counterparts in paper I (see the perspectives of improvement in Section 5.4). Still, we emphasize that the planet mass estimates reported in this study are obtained using a fully independent method to that used in paper I. Therefore, having consistent planet mass estimates between the two studies reinforces the robustness of the planet detection from the HARPS data set.

Similarly to paper I, the masses of AU Mic b and AU Mic c are respectively found slightly lower and significantly larger than their counterparts in Cale et al. (2021), who conducted a velocimetric analysis of a large number of data points collected with multiple optical and nIR spectrographs. The origin of this discrepancy, discussed in more details in the section 4.1 of paper I, remains unclear. Hence the need to (i) continue the dense RV follow-up of the AU Mic system using different high-precision velocimeters and (ii) carry out independent analyses led by different teams.

Our mass estimates follow the same trend as those reported in paper I, i.e. AU Mic c, although smaller than planet b, is significantly more massive. Potential planet formation and evolution scenarios are discussed in detail in the section 4.5 of paper I. One of the main outcomes of this analysis is that the bulk densities of the two planets appear to be in tension with standard core accretion scenarios (e.g. Pollack et al. 1996; Lee & Chiang 2015). First, both planets seem to have accreted less H/He from their parent disc than predicted by standard core accretion models. Secondly, the origin of the high density of planet c is hard to reconcile with planet formation and evolution models given that more massive cores are expected to accrete more H/He in standard core accretion scenarios. These results confirm the crucial need to obtain precise estimates of the mean inner densities of planets transiting very young PMS stars (e.g. K2-33, V1298 Tau, HIP 67522 TOI 1227, reported in David et al. 2016, 2019; Rizzuto et al. 2020; Mann et al. 2021; Suárez Mascareño et al. 2021, respectively), in order to resolve potential systematic discrepancies between planet formation and evolution models and the observations.

5.3 Stellar activity and differential rotation

The DI process yields respective spot coverages of 4.7 per cent and 5.1 per cent for the 2020 and 2021 periods, ∼3.5 times larger than the 1.4 per cent obtained from the spectra collected in 2019 with the near-infrared (nIR) spectropolarimeter SPIRou (Klein et al. 2021). This increase is almost twice as large as that expected by rescaling our brightness distributions by the Planck's law to account for the decrease in feature contrast between the optical and nIR spectral domains (see fig. 6 of Cale et al. 2021). This excess of spot coverage might either indicate a significant evolution of the stellar activity since 2019 or reflect the fact that the line profile distortions do not trace the same physical phenomena in the nIR, more sensitive to the small-scale field as highlighted in Klein et al. (2021). Once again, spectropolarimetric observations are needed to constrain the strength and topology of the large-scale magnetic field of AU Mic and disentangle between the two scenarios.

We detect a weak DR of $d\Omega = 0.01\,rad\,d^{-1}$ shearing the 2021 brightness distribution of AU Mic, whereas the 2020 counterpart is consistent with a solid-body rotation. These values are significantly weaker than the DR level of $d\Omega = 0.075 \pm 0.031\,rad\,d^{-1}$ detected from the SPIRou nIR unpolarized line profiles collected in 2019 (Klein et al. 2021). We caution that, since most of the features reconstructed with DI are located near the stellar equator (see Fig. 7), our weak DR estimate might just reflect the partial latitudinal coverage of our brightness maps. We investigate this effect from synthetic CCFs created from the best-fitting brightness distributions shown in Fig. 7. For each period (i.e. 2020 and 2021), we generate 20 mock CCF time-series assuming different level of DR, from $d\Omega = 0$ to $0.17\,rad\,d^{-1}$ (corresponding to the level DR detected from the large-scale magnetic field in Kl21), and inject random noise at the same level as in our observations. In order to assess whether a hypothetical DR would have been detected in our data, we apply our DI code on all these data sets using the method described in Section 4.1, and estimate the significance of a model at the best-fitting DR parameters compared to a model assuming a solid-body rotation. This process is then repeated for 10 different realizations of white noise. For both 2020 and 2021 periods, we find that a DR would have been accurately detected at a significance larger than 5σ. We therefore discard strong biases towards low DR values from our actual DI reconstructions. However, once again, it is difficult to draw conclusions about the DR evolution from the 2019 SPIRou observations of AU Mic and our HARPS observations. As outlined in Klein et al. (2021), the activity-induced distortions of the intensity line profiles observed with SPIRou are most likely of magnetic origin, whereas the variations of HARPS CCFs are primarily due to contrast effects (as expected from the youth and late spectral type of AU Mic; e.g. Hébrard et al. 2014; Beeck et al. 2015; Baroch et al. 2020; Panja, Cameron & Solanki 2020). As a consequence, one alternative explanation for the observed discrepancy in DR is that the brightness distribution probed by HARPS CCFs is anchored at a different depth of the convective zone than the small-scale magnetic field probed by the SPIRou line profiles.

We also note that the time-series of chromospheric indices are primarily modulated at rotation periods of typically 4.80 ± 0.01 d (see Section 2), which cannot be directly reconciled with the rotation periods unveiled from the observed HARPS CCFs (equatorial periods of 4.85 ± 0.01 and 4.8559 ± 0.0009 d in 2020 and 2021, respectively). Since the non-radiative chromospheric emission is more sensitive to the surface magnetic field of the star, it reinforces the idea that the small-scale magnetic field probes slightly different layers of the stellar interior in the case of AU Mic. We note that a contemporary spectropolarimetric monitoring of AU Mic using both optical (e.g. HARPS-Pol, ESPaDOnS, and Neo-NARVAL) and nIR (e.g. SPIRou and CRIRES+) should be able to confirm or infirm this assumption. Moreover, the magnetic properties derived from time-series of circularly polarized Zeeman signatures with Zeeman–Doppler imaging have been shown to be excellent proxies of solar-like magnetic cycles (Lehmann et al. 2021). Monitoring the long-term evolution of the large-scale field at the surface of AU Mic will allow us to (i) unveil the origin of the discrepancies in spot coverage and latitudinal DR between HARPS and SPIRou observations and

Downloaded from https://academic.oup.com/mnras/article/512/4/5067/6552137 by guest on 19 May 2022

(ii) help investigate the nature of the putative 5-yr activity cycle reported in Ibañez Bustos et al. (2019).

5.4 Perspectives: filtering stellar activity using Doppler Imaging

This study confirms that DI has the potential to be used as a reliable independent alternative to the search for planet signatures in RV time-series, as it leverages both the spectral and temporal information available in the CCFs to model activity-induced profile distortions whilst leaving planet-induced profile shifts untouched (similarly to what is done in Collier Cameron et al. 2021, but with a more physically motivated approach). For the time being, our DI code has been shown to give reliable estimates of close-in planet velocimetric parameters provided that (i) the star's rotation cycle is densely observed on time-scales on which the stellar activity does not significantly evolve, (ii) the star rotates relatively fast ($v \sin i_{\rm rot} \gtrsim 10\,{\rm km\,s^{-1}}$), (iii) the noise level in the observed CCFs is low enough to resolve the profile distortions, and (iv) the total duration of the observations is significantly larger than the planet orbital period.

However, reliable prospects for overcoming these limitations seem to be emerging. First and foremost, including the intrinsic evolution of the brightness topology, for example, by coupling the DI reconstruction to a stochastic process (as proposed by Yu et al. 2019; Finociety et al. 2021; Luger et al. 2021, and Finociety et al., in preparation) will help increase the model flexibility and, thus, will allow one to combine more observations in the DI reconstruction process, thereby obtaining more precise estimates of star/planet parameters. Secondly, recent efforts to solve the DI inversion in the Bayesian framework suggests that a robust exploration of the parameter space, not dependent on the initial conditions and not affected by local χ^2 minimums, might soon be permitted in the DI framework (Asensio Ramos, Diaz Baso & Kochukhov 2022). Finally, we emphasize that DI can be applied to slow rotators, as already demonstrated in Hébrard et al. (2016), as long as the observations are precise-enough to resolve the activity-induced profile distortions and densely cover the stellar rotation cycle. Systematic differences between the intrinsic profile used in the DI code and the observed CCFs have been shown to be efficiently removed through the iterative process described in Klein et al. (2021).

Under these conditions, it becomes conceivable to apply DI to model the profile distortion of solar-like stars and search for planets around them. However, the activity-induced profile distortions of these stars are known to be primarily affected by the inhibition of convective blueshift in active regions rather than by changes in contrast of the photospheric brightness (e.g. Meunier, Desort & Lagrange 2010; Milbourne et al. 2019). Such effects can be easily incorporated to DI as demonstrated by Hébrard et al. (2016), by redshifting local profiles within regions of strong magnetic field in the reconstruction process. It may therefore be possible to invert a time-series of CCFs into surface distributions of relative brightness (spots/plages) and local redshift (i.e. corresponding to regions where the inhibition of convective blueshift is maximum). Since both effects have been shown to affect different spectral lines (e.g. Cretignier et al. 2020), it might be possible to produce two CCF time-series, each primarily affected by one physical process, and to simultaneously invert them into two different maps while searching for the same planet signatures in both time-series (as proposed by Meunier, Lagrange & Borgniet 2017). The high-resolution solar spectra collected as a part of an intensive monitoring campaign with HARPS-N (Dumusque et al. 2015; Collier Cameron et al. 2019; Dumusque et al. 2021) is the ideal benchmark for testing and validating these new methods (e.g. by comparing the resulting maps with data products from the Solar Dynamics Observatory; Pesnell, Thompson & Chamberlin 2012; Haywood et al. 2016, 2020). Applying these methods to other solar-type stars will require to follow them up intensely with state-of-the-art spectrometers as proposed, for example, by the Terra Hunting Experiment[6] (Hall et al. 2018).

ACKNOWLEDGEMENTS

We gratefully acknowledge X. Dumusque and F. Bouchy for their coordination of the HARPS time-share, which allowed us to spread the observations over the two semesters with the appropriate time-sampling, and all the observers involved in the time-share (F. Bouchy, B. Canto, I. de Castro, G. Dransfield, M. Esposito, V. Van Eylen, F. Hawthorn, M. Hobson, V. Hodzic, D. Martin, J. McCormac, H. Os-borne, J. Otegi, A. Suarez, and P. Torres) for carrying out the observations on our behalf. We also thank J. Patterson for managing the Oxford Astrophysics compute cluster, glamdring, which was used to carry out the data analysis. This study is based on observations collected at the European Southern Observatory under ESO programmes 0105.C-0288[7] & 0106.C-0852 (PIs Aigrain and Zicher). This research has made use of NASA's Astrophysics Data System. KB, BO, and AS acknowledge funding from the European Research Council under the European Union's Horizon 2020 research and innovation programme (grant agreement no. 865624, GPRV). NZ acknowledges support from the UK Science and Technology Facilities Council (STFC) under Grant Code ST/N504233/1, studentship no. 1947725. AAV and RDK acknowledge funding from the European Research Council (ERC) under the European Union's Horizon 2020 research and innovation programme (grant agreement no. 817540, ASTROFLOW). LDN thanks the Swiss National Science Foundation for support under Early Postdoc.Mobility grant P2GEP2_200044. AS acknowledges PLATO CNES funding at CEA/IFU/DAp and funding from the Programme National de Planétologie (PNP). BN's work is supported by STFC Consolidated Grant ST/S000488/1 (PI Balbus). JFD and JB acknowledge funding from the ERC under the H2020 research and innovation programme (grant agreements no. 740651 NewWorlds, and no. 742095 SPIDI: Star-Planets-Inner Disk-Interactions). Finally, we thank the reviewer for valuable comments and suggestions which helped us improving an earlier version of the manuscript.

DATA AVAILABILITY

The HARPS spectra used in this study are available on the ESO archive.[8]

REFERENCES

Addison B. C. et al., 2020, AJ, 162, 137
Afram N., Berdyugina S. V., 2019, A&A, 629, A83
Asensio Ramos A., Diaz Baso C., Kochukhov O., 2022, A&A, 658, 162
Astropy Collaboration, 2013, A&A, 558, A33
Astropy Collaboration, 2018, AJ, 156, 123
Baluev R. V., 2008, MNRAS, 385, 1279
Baroch D. et al., 2020, A&A, 641, A69
Barragán O., Aigrain S., Rajpaul V. M., Zicher N., 2022, MNRAS, 509, 866

[6] http://www.terrahunting.org/index.html
[7] The P105 observations were delayed because of the COVID-19 pandemic and taken in P107.
[8] http://archive.eso.org/eso/eso_archive_main.html

Downloaded from https://academic.oup.com/mnras/article/512/4/5067/6552137 by guest on 19 May 2022

Baruteau C., Bai X., Mordasini C., Mollière P., 2016, Space Sci. Rev., 205, 77
Beeck B., Schüssler M., Cameron R. H., Reiners A., 2015, A&A, 581, A42
Berdyugina S. V., 2005, Living Rev. Sol. Phys., 2, 8
Boisse I. et al., 2009, A&A, 495, 959
Bonfils X. et al., 2007, A&A, 474, 293
Bonfils X. et al., 2013, A&A, 549, A109
Bouvier J., Bertout C., 1989, A&A, 211, 99
Bouvier J. et al., 2007, A&A, 463, 1017
Brown S. F., Donati J. F., Rees D. E., Semel M., 1991, A&A, 250, 463
Cale B. L. et al., 2021, AJ, 162, 295
Cauley P. W., Shkolnik E. L., Llama J., Bourrier V., Moutou C., 2018, AJ, 156, 262
Cauley P. W., Shkolnik E. L., Llama J., Lanza A. F., 2019, Nature Astron., 3, 1128
Claret A., Bloemen S., 2011, A&A, 529, A75
Collier Cameron A. et al., 2019, MNRAS, 487, 1082
Collier Cameron A. et al., 2021, MNRAS, 505, 1699
Cretignier M., Dumusque X., Allart R., Pepe F., Lovis C., 2020, A&A, 633, A76
Crockett C. J., Mahmud N. I., Prato L., Johns-Krull C. M., Jaffe D. T., Hartigan P. M., Beichman C. A., 2012, ApJ, 761, 164
Cuntz M., Saar S. H., Musielak Z. E., 2000, ApJ, 533, L151
David T. J. et al., 2016, Nature, 534, 658
David T. J., Petigura E. A., Luger R., Foreman-Mackey D., Livingston J. H., Mamajek E. E., Hillenbrand L. A., 2019, ApJ, 885, L12
Donati J. F., Brown S. F., 1997, A&A, 326, 1135
Donati J. F., Landstreet J. D., 2009, ARA&A, 47, 333
Donati J. F., Mengel M., Carter B. D., Marsden S., Collier Cameron A., Wichmann R., 2000, MNRAS, 316, 699
Donati J. F. et al., 2014, MNRAS, 444, 3220
Donati J. F. et al., 2016, Nature, 534, 662
Donati J. F. et al., 2017, MNRAS, 465, 3343
Dumusque X. et al., 2015, ApJ, 814, L21
Dumusque X. et al., 2021, A&A, 648, A103
Fares R. et al., 2010, MNRAS, 406, 409
Finociety B. et al., 2021, MNRAS, 508, 3427
Fischer C., Saur J., 2019, ApJ, 872, 113 (F19)
Gaia Collaboration, 2018, A&A, 616, A1
Gomes da Silva J., Santos N. C., Bonfils X., Delfosse X., Forveille T., Udry S., 2011, A&A, 534, A30
Hall R. D., Thompson S. J., Handley W., Queloz D., 2018, MNRAS, 479, 2968
Haywood R. D. et al., 2014, MNRAS, 443, 2517
Haywood R. D. et al., 2016, MNRAS, 457, 3637
Haywood R. D. et al., 2020, preprint (arXiv:2005.13386)
Hebb L., Petro L., Ford H. C., Ardila D. R., Toledo I., Minniti D., Golimowski D. A., Clampin M., 2007, MNRAS, 379, 63
Hébrard É. M., Donati J. F., Delfosse X., Morin J., Boisse I., Moutou C., Hébrard G., 2014, MNRAS, 443, 2599
Hébrard É. M., Donati J. F., Delfosse X., Morin J., Moutou C., Boisse I., 2016, MNRAS, 461, 1465
Heitzmann A. et al., 2021, MNRAS, 505, 4989
Hirano T. et al., 2020, ApJ, 899, L13
Ibañez Bustos R. V., Buccino A. P., Flores M., Martinez C. I., Maizel D., Messina S., Mauas P. J. D., 2019, MNRAS, 483, 1159
Ip W.-H., Kopp A., Hu J.-H., 2004, ApJ, 602, L53
Johns C. M., Basri G., 1995, AJ, 109, 2800
Kavanagh R. D. et al., 2019, MNRAS, 485, 4529
Kavanagh R. D., Vidotto A. A., Klein B., Jardine M. M., Donati J.-F., Ó Fionnagáin D., 2021, MNRAS, 504, 1511
Klein B. et al., 2021, MNRAS, 502, 188
Kochukhov O., 2016, in Lecture Notes in Physics, Vol. 914, Cartography of the Sun and the Stars.. Springer, Cham, p. 177
Lanza A. F., 2009, A&A, 505, 339
Lanza A. F., 2013, A&A, 557, A31
Lanza A. F., 2018, A&A, 610, A81
Lee E. J., Chiang E., 2015, ApJ, 811, 41
Lehmann L. T., Hussain G. A. J., Vidotto A. A., Jardine M. M., Mackay D. H., 2021, MNRAS, 500, 1243
Luger R., Bedell M., Foreman-Mackey D., Crossfield I. J. M., Zhao L. L., Hogg D. W., 2021, preprint (arXiv:2110.06271)
MacGregor A. M., Osten R. A., Hughes A. M., 2020, ApJ, 891, 80
Madhusudhan N., 2019, ARA&A, 57, 617
Malo L. et al., 2014, ApJ, 792, 37
Mamajek E. E., Bell C. P. M., 2014, MNRAS, 445, 2169
Mann A. W. et al., 2016a, AJ, 152, 61
Mann A. W. et al., 2016b, ApJ, 818, 46
Mann A. W. et al., 2021, AJ, 163, 156
Martioli E. et al., 2020, A&A, 641, L1
Martioli E., Hébrard G., Correia A. C. M., Laskar J., Lecavelier des Etangs A., 2021, A&A, 649, A177
Mayor M. et al., 2003, The Messenger, 114, 20
Messina S. et al., 2016, A&A, 596, A29
Meunier N., Desort M., Lagrange A. M., 2010, A&A, 512, A39
Meunier N., Lagrange A. M., Borgniet S., 2017, A&A, 607, A6
Milbourne T. W. et al., 2019, ApJ, 874, 107
Mordasini C., Alibert Y., Georgy C., Dittkrist K. M., Klahr H., Henning T., 2012, A&A, 547, A112
Owen J. E., Wu Y., 2017, ApJ, 847, 29
Palle E. et al., 2020, A&A, 643, A25
Panja M., Cameron R., Solanki S. K., 2020, ApJ, 893, 113
Pesnell W. D., Thompson B. J., Chamberlin P. C., 2012, Sol. Phys., 275, 3
Petit P., Donati J. F., Collier Cameron A., 2002, MNRAS, 334, 374
Petit P. et al., 2015, A&A, 584, A84
Plavchan P., Werner M. W., Chen C. H., Stapelfeldt K. R., Su K. Y. L., Stauffer J. R., Song I., 2009, ApJ, 698, 1068
Plavchan P. et al., 2020, Nature, 582, 497
Pollack J. B., Hubickyj O., Bodenheimer P., Lissauer J. J., Podolak M., Greenzweig Y., 1996, Icarus, 124, 62
Press W. H., Teukolsky S. A., Vetterling W. T., Flannery B. P., 1992, Numerical Recipes in FORTRAN. The Art of Scientific Computing. Cambridge Univ. Press, Cambridge
Queloz D. et al., 2001, A&A, 379, 279
Rajpaul V., Aigrain S., Osborne M. A., Reece S., Roberts S., 2015, MNRAS, 452, 2269
Raymond S. N., Morbidelli A., 2020, preprint (arXiv:2002.05756)
Rizzuto A. C. et al., 2020, AJ, 160, 33
Robinson R. D., Linsky J. L., Woodgate B. E., Timothy J. G., 2001, ApJ, 554, 368
Rodono M. et al., 1986, A&A, 165, 135
Saar S. H., Cuntz M., 2001, MNRAS, 325, 55
Saur J., Grambusch T., Duling S., Neubauer F. M., Simon S., 2013, A&A, 552, A119
Semel M., 1989, A&A, 225, 456
Skilling J., Bryan R. K., 1984, MNRAS, 211, 111
Sousa A. P. et al., 2021, A&A, 649, A68
Strugarek A., 2018, in Deeg H. J., Belmonte J. A., eds, Handbook of Exoplanets. Springer,Cham, p. 25
Strugarek A., Brun A. S., Donati J. F., Moutou C., Réville V., 2019, ApJ, 881, 136
Strugarek A. et al., 2022, preprint (arXiv:2203.10956)
Suárez Mascareño A. et al., 2021, Nat. Astron., 6, 232
Torres C. A. O., Ferraz Mello S., 1973, A&A, 27, 231
Unno W., 1956, PASJ, 8, 108
Vogt S. S., Penrod G. D., Hatzes A. P., 1987, ApJ, 321, 496
Weise P., Launhardt R., Setiawan J., Henning T., 2010, A&A, 517, A88
White R., Schaefer G., Boyajian T., von Braun K., ten Brummelaar T., Bieryla A., Dupuy T., Latham D. W., 2019, in American Astronomical Society, AAS Meeting #233, p. 259.41
Wood B. E., Müller H. R., Zank G. P., Linsky J. L., Redfield S., 2005, ApJ, 628, L143
Yu L. et al., 2017, MNRAS, 467, 1342
Yu L. et al., 2019, MNRAS, 489, 5556
Zechmeister M., Kürster M., 2009, A&A, 496, 577
Zechmeister M. et al., 2018, A&A, 609, A12
Zicher N. et al., 2022, MNRAS, 512, 3060

Downloaded from https://academic.oup.com/mnras/article/512/4/5067/6552137 by guest on 19 May 2022

APPENDIX A: JOURNAL OF OBSERVATIONS

The full journal of observations, including the observation dates, noise values in the CCFs, RV/FWHM/BIS time-series, and the chromospheric activity indices computed in Section 3.1, is given in Table A1.

APPENDIX B: ACTIVITY PROXIES

B1 Chromospheric emission lines

The observed Ca II H & K, Hα, Hβ, Na I D1 & D2, and He I D3 profiles are shown in units of blaze-corrected flux in the stellar rest frame in Fig. B1.

Table A1. Journal of HARPS observations analysed in this study. The first four columns respectively list the UT date, the BJD at mid-exposure of each observation, the SNR at 550 nm, and the RMS noise level in the CCF. Column 5 indicates spectra polluted by the Moon or affected by a stellar flare. The time-series of DRS-provided RVs, FWHM, and BIS are respectively listed in columns 6–8 (we adopt a typical error bar of 15 m s^{-1} for the FWHM and BIS values). Finally, we give chromospheric emission indices based on Ca II H & K (3968.47 and 3933.66 Å), Hα (6562.808 Å), Hβ (4861.363 Å), Na I D1 & D2 (5895.92 and 5889.95 Å), and He I D3 (5875.62 Å) in the last five columns.

UT Date	BJD	S/N	σ_{CCF}	Comments	RV	FWHM	BIS	$S_{Ca\,II}$	Hα	Hβ	Na I	He I
–	(BJD$_{TDB}$ − 2 457 000)	–	($\times 10^{-4}$)	–	(km s^{-1})	(km s^{-1})	(km s^{-1})	–	–	–	–	–
2020-11-15	2168.59981	75.1	4.7		−4.622 ± 0.007	10.54	−0.16	9.2606 ± 0.0081	1.9408 ± 0.0001	2.4122 ± 0.0004	0.2108 ± 0.0001	1.1860 ± 0.0002
2020-11-17	2170.58023	59.2	5.8		−4.786 ± 0.009	10.78	−0.02	9.8289 ± 0.0107	2.0960 ± 0.0001	2.6658 ± 0.0006	0.2272 ± 0.0001	1.2065 ± 0.0003
2020-11-18	2171.54293	73.2	4.8		−4.669 ± 0.007	10.73	−0.03	9.6329 ± 0.0076	2.0447 ± 0.0001	2.5515 ± 0.0004	0.2170 ± 0.0001	1.2012 ± 0.0002
2020-11-19	2172.53450	108.9	3.3		−4.928 ± 0.005	10.71	0.09	9.5134 ± 0.0050	1.9959 ± 0.0001	2.5150 ± 0.0002	0.2181 ± 0.0001	1.1997 ± 0.0001
2020-11-22	2175.50735	101.4	3.5		−4.771 ± 0.005	10.76	−0.03	9.7041 ± 0.0052	2.0872 ± 0.0001	2.6374 ± 0.0003	0.2253 ± 0.0001	1.2074 ± 0.0001
2020-11-22	2175.56221	84.9	4.2		−4.773 ± 0.006	10.80	−0.05	9.9363 ± 0.0072	2.1216 ± 0.0001	2.7238 ± 0.0003	0.2313 ± 0.0001	1.2220 ± 0.0002
2020-11-23	2176.50801	99.4	3.6		−4.671 ± 0.005	10.77	−0.03	9.7568 ± 0.0054	2.1079 ± 0.0001	2.6359 ± 0.0003	0.2243 ± 0.0001	1.2035 ± 0.0001
2020-11-24	2177.51177	107.9	3.4		−4.964 ± 0.005	10.67	0.12	9.7824 ± 0.0053	2.0319 ± 0.0001	2.6041 ± 0.0002	0.2263 ± 0.0001	1.2027 ± 0.0001
2020-11-25	2178.50720	93.0	3.9		−4.623 ± 0.006	10.67	−0.17	10.1740 ± 0.0059	2.1333 ± 0.0001	2.7701 ± 0.0003	0.2353 ± 0.0001	1.2170 ± 0.0001
2020-11-25	2178.51843	88.2	4.0		−4.629 ± 0.006	10.69	−0.15	10.2684 ± 0.0065	2.1341 ± 0.0001	2.7660 ± 0.0003	0.2348 ± 0.0001	1.2165 ± 0.0002
2020-11-26	2179.51743	114.1	–	Flare	−4.762 ± 0.005	10.79	−0.07	12.9278 ± 0.0062	2.4398 ± 0.0001	3.3473 ± 0.0002	0.2927 ± 0.0001	1.2704 ± 0.0001
2020-11-27	2180.54004	107.1	3.4		−4.749 ± 0.005	10.81	−0.02	11.0421 ± 0.0062	2.2608 ± 0.0001	2.9794 ± 0.0003	0.2526 ± 0.0001	1.2179 ± 0.0001
2020-11-28	2181.54053	86.0	4.2		−4.732 ± 0.006	10.83	0.02	11.4547 ± 0.0074	2.3659 ± 0.0001	3.1749 ± 0.0004	0.2637 ± 0.0001	1.2759 ± 0.0002
2020-11-29	2182.53789	108.6	3.4		−4.923 ± 0.005	10.53	0.14	9.7686 ± 0.0059	1.9993 ± 0.0001	2.5468 ± 0.0003	0.2206 ± 0.0001	1.1954 ± 0.0001
2020-11-30	2183.54048	123.3	3.0		−4.657 ± 0.004	10.77	−0.07	10.7131 ± 0.0049	2.2642 ± 0.0001	2.9157 ± 0.0002	0.2485 ± 0.0001	1.2664 ± 0.0001
2020-12-01	2184.54177	126.7	2.9		−4.813 ± 0.004	10.83	−0.00	10.3151 ± 0.0048	2.2843 ± 0.0001	2.8855 ± 0.0002	0.2356 ± 0.0001	1.2284 ± 0.0001
2020-12-02	2185.54211	73.8	4.8		−4.727 ± 0.007	10.78	0.01	10.0738 ± 0.0083	2.1483 ± 0.0001	2.7128 ± 0.0004	0.2280 ± 0.0001	1.2093 ± 0.0002
2020-12-05	2188.54816	95.4	3.8		−4.716 ± 0.005	10.71	−0.02	9.4786 ± 0.0055	2.0197 ± 0.0001	2.5273 ± 0.0003	0.2157 ± 0.0001	1.1948 ± 0.0001
2020-12-06	2189.54737	122.6	3.0		−4.861 ± 0.004	10.81	0.07	11.5011 ± 0.0048	2.3254 ± 0.0001	3.1736 ± 0.0002	0.2676 ± 0.0001	1.2666 ± 0.0001
2020-12-07	2190.52211	110.7	3.3		−4.720 ± 0.005	10.79	0.07	10.8230 ± 0.0047	2.2854 ± 0.0001	3.0350 ± 0.0002	0.2484 ± 0.0001	1.2706 ± 0.0001
2020-12-08	2191.52198	128.9	2.9		−4.834 ± 0.004	10.81	0.10	10.4088 ± 0.0049	2.1643 ± 0.0001	2.8234 ± 0.0002	0.2331 ± 0.0001	1.2213 ± 0.0001
2020-12-09	2192.52110	128.5	2.9		−4.808 ± 0.004	10.41	0.03	10.2756 ± 0.0046	2.1205 ± 0.0001	2.6961 ± 0.0002	0.2320 ± 0.0001	1.1999 ± 0.0001
2021-05-24	2358.80511	138.8	2.9		−4.560 ± 0.004	10.74	−0.18	10.0506 ± 0.0030	2.0604 ± 0.0001	2.7077 ± 0.0002	0.2389 ± 0.0001	1.2207 ± 0.0001
2021-05-25	2359.75665	120.3	3.3		−4.792 ± 0.004	10.52	0.02	9.3572 ± 0.0038	2.0587 ± 0.0001	2.5386 ± 0.0002	0.2239 ± 0.0001	1.2071 ± 0.0001
2021-05-25	2359.87440	122.8	3.2		−4.714 ± 0.004	10.58	−0.06	9.2266 ± 0.0031	2.0251 ± 0.0001	2.4693 ± 0.0002	0.2203 ± 0.0001	1.1951 ± 0.0001
2021-05-26	2360.76126	115.6	3.4		−4.714 ± 0.005	10.86	−0.01	9.5844 ± 0.0039	2.1051 ± 0.0001	2.6118 ± 0.0002	0.2266 ± 0.0001	1.2040 ± 0.0001
2021-05-26	2360.88080	95.4	4.0		−4.756 ± 0.005	10.84	0.04	9.8530 ± 0.0044	2.1402 ± 0.0001	2.6966 ± 0.0003	0.2343 ± 0.0001	1.2188 ± 0.0001
2021-05-27	2361.78805	84.8	4.6		−4.943 ± 0.006	10.71	0.13	9.7470 ± 0.0053	2.1024 ± 0.0001	2.6250 ± 0.0004	0.2292 ± 0.0001	1.2214 ± 0.0002
2021-06-01	2366.73319	111.0	3.5		−4.978 ± 0.005	10.68	0.12	9.7278 ± 0.0041	2.0791 ± 0.0001	2.5945 ± 0.0002	0.2251 ± 0.0001	1.2095 ± 0.0001
2021-06-01	2366.85758	86.2	4.3		−4.944 ± 0.006	10.64	0.07	10.4283 ± 0.0047	2.1398 ± 0.0001	2.7547 ± 0.0003	0.2366 ± 0.0001	1.2240 ± 0.0002
2021-06-02	2367.73664	97.9	4.0		−4.857 ± 0.005	10.63	0.10	10.7515 ± 0.0050	2.1716 ± 0.0001	2.8956 ± 0.0003	0.2548 ± 0.0001	1.2720 ± 0.0001
2021-06-02	2367.84344	87.9	4.3		−4.784 ± 0.006	10.52	0.04	10.9900 ± 0.0054	2.2166 ± 0.0001	2.9121 ± 0.0003	0.2600 ± 0.0001	1.2682 ± 0.0001
2021-06-03	2368.81209	110.8	3.5		−4.711 ± 0.005	10.99	−0.02	9.0297 ± 0.0037	1.9376 ± 0.0001	2.3695 ± 0.0002	0.2153 ± 0.0001	1.1890 ± 0.0001
2021-06-03	2368.91402	107.5	3.7		−4.785 ± 0.005	10.95	0.04	9.2627 ± 0.0049	1.9917 ± 0.0001	2.5019 ± 0.0003	0.2229 ± 0.0001	1.2151 ± 0.0001
2021-06-04	2369.79091	131.8	2.9		−4.615 ± 0.004	10.70	−0.13	9.9850 ± 0.0030	2.0953 ± 0.0001	2.6691 ± 0.0002	0.2319 ± 0.0001	1.2182 ± 0.0001
2021-06-04	2369.92061	120.4	3.3		−4.603 ± 0.004	10.79	−0.10	9.3959 ± 0.0043	2.0505 ± 0.0001	2.5908 ± 0.0002	0.2218 ± 0.0001	1.2038 ± 0.0001
2021-06-05	2370.76677	83.5	4.6		−4.774 ± 0.006	10.82	0.01	9.9179 ± 0.0052	2.1579 ± 0.0001	2.7223 ± 0.0004	0.2308 ± 0.0001	1.2124 ± 0.0002
2021-06-06	2371.78083	124.1	–	Flare	−4.930 ± 0.004	10.71	0.06	12.5039 ± 0.0039	2.5356 ± 0.0001	3.5115 ± 0.0002	0.2844 ± 0.0001	1.3054 ± 0.0001
2021-06-06	2371.90653	113.8	3.6		−4.921 ± 0.005	10.65	0.06	10.4133 ± 0.0050	2.2920 ± 0.0001	2.9205 ± 0.0003	0.2420 ± 0.0001	1.2244 ± 0.0001
2021-06-07	2372.75324	92.7	4.2		−4.778 ± 0.006	10.48	0.05	9.7121 ± 0.0048	2.0316 ± 0.0001	2.5870 ± 0.0003	0.2317 ± 0.0001	1.2100 ± 0.0001
2021-06-11	2376.72259	108.6	3.6		−4.922 ± 0.005	10.62	0.05	10.6094 ± 0.0044	2.1554 ± 0.0001	2.7781 ± 0.0003	0.2423 ± 0.0001	1.2192 ± 0.0001
2021-06-12	2377.74066	120.9	3.2		−4.711 ± 0.004	10.44	0.01	10.8036 ± 0.0038	2.1599 ± 0.0001	2.7811 ± 0.0002	0.2509 ± 0.0001	1.2341 ± 0.0001
2021-06-13	2378.78840	115.3	3.4		−4.859 ± 0.005	10.82	0.12	9.7233 ± 0.0036	1.9942 ± 0.0001	2.4764 ± 0.0002	0.2237 ± 0.0001	1.2014 ± 0.0001
2021-06-14	2379.86158	90.8	4.3		−4.652 ± 0.006	10.82	−0.08	10.2452 ± 0.0057	2.2032 ± 0.0001	2.9424 ± 0.0003	0.2517 ± 0.0001	1.2620 ± 0.0001
2021-07-10	2405.78455	122.2	3.2		−4.968 ± 0.004	10.56	0.08	11.0842 ± 0.0041	2.2592 ± 0.0001	2.9694 ± 0.0002	0.2577 ± 0.0001	1.2597 ± 0.0001
2021-07-11	2406.71022	72.1	5.3		−4.815 ± 0.007	10.54	0.12	9.5724 ± 0.0065	1.9712 ± 0.0001	2.4489 ± 0.0004	0.2229 ± 0.0001	1.1952 ± 0.0002
2021-07-13	2408.90951	66.2	5.9		−4.611 ± 0.008	10.79	−0.13	9.6850 ± 0.0101	2.0544 ± 0.0001	2.5845 ± 0.0006	0.2252 ± 0.0001	1.2019 ± 0.0002
2021-07-14	2409.71290	81.4	4.8		−4.778 ± 0.007	10.82	−0.05	10.8055 ± 0.0062	2.2442 ± 0.0001	2.9478 ± 0.0004	0.2567 ± 0.0001	1.2479 ± 0.0002
2021-07-15	2410.70717	93.6	4.1		−4.962 ± 0.005	10.60	0.05	10.1279 ± 0.0046	2.0802 ± 0.0001	2.6175 ± 0.0003	0.2346 ± 0.0001	1.2121 ± 0.0001
2021-07-15	2410.79291	93.7	4.2		−4.931 ± 0.006	10.62	0.02	11.0440 ± 0.0061	2.1888 ± 0.0001	2.9409 ± 0.0003	0.2580 ± 0.0001	1.2366 ± 0.0001
2021-07-16	2411.74121	121.3	3.2		−4.697 ± 0.004	10.45	0.02	9.1095 ± 0.0030	1.9407 ± 0.0001	2.3077 ± 0.0002	0.2139 ± 0.0001	1.1811 ± 0.0001
2021-07-17	2412.62503	101.8	3.8		−4.697 ± 0.005	10.96	−0.01	10.0047 ± 0.0043	2.0583 ± 0.0001	2.5822 ± 0.0003	0.2287 ± 0.0001	1.2244 ± 0.0001
2021-07-17	2412.74029	92.4	4.1		−4.762 ± 0.006	10.90	0.05	10.0587 ± 0.0046	2.0736 ± 0.0001	2.6265 ± 0.0003	0.2368 ± 0.0001	1.2263 ± 0.0001
2021-07-27	2422.69852	78.7	4.9		−4.859 ± 0.007	10.71	0.08	11.1785 ± 0.0070	2.2552 ± 0.0001	3.0334 ± 0.0004	0.2619 ± 0.0001	1.2826 ± 0.0002
2021-07-27	2422.83670	72.3	5.5		−4.834 ± 0.007	10.63	0.03	11.1212 ± 0.0093	2.3507 ± 0.0001	3.1260 ± 0.0005	0.2685 ± 0.0001	1.2889 ± 0.0002
2021-07-28	2423.70035	71.0	–	Flare	−4.721 ± 0.008	10.95	−0.02	15.1729 ± 0.0082	2.9270 ± 0.0002	4.0772 ± 0.0005	0.4098 ± 0.0001	1.5472 ± 0.0002
2021-07-28	2423.79786	76.6	–	Flare	−4.756 ± 0.007	10.90	0.05	13.8001 ± 0.0092	2.6731 ± 0.0001	3.7837 ± 0.0005	0.3484 ± 0.0001	1.3922 ± 0.0002
2021-07-29	2424.73029	117.2	3.3		−4.969 ± 0.005	10.92	0.12	10.6437 ± 0.0038	2.2041 ± 0.0001	2.7893 ± 0.0002	0.2449 ± 0.0001	1.2269 ± 0.0001
2021-07-30	2425.66184	92.9	4.1		−4.874 ± 0.006	10.67	0.01	9.9614 ± 0.0047	2.0396 ± 0.0001	2.5177 ± 0.0003	0.2289 ± 0.0001	1.1981 ± 0.0001
2021-07-31	2426.61526	80.8	4.6		−4.534 ± 0.006	10.48	−0.11	10.0349 ± 0.0053	2.0393 ± 0.0001	2.5706 ± 0.0004	0.2301 ± 0.0001	1.2145 ± 0.0002
2021-08-01	2427.77361	122.4	3.2		−4.818 ± 0.004	10.66	0.05	9.4127 ± 0.0039	2.0613 ± 0.0001	2.5355 ± 0.0002	0.2202 ± 0.0001	1.1958 ± 0.0001
2021-08-02	2428.82886	106.6	–	Flare	−4.831 ± 0.005	10.78	0.13	14.0563 ± 0.0068	2.6252 ± 0.0001	3.7482 ± 0.0003	0.3232 ± 0.0001	1.3275 ± 0.0001
2021-08-03	2429.75989	90.0	4.3		−5.034 ± 0.006	10.78	0.20	10.5755 ± 0.0055	2.1168 ± 0.0001	2.7080 ± 0.0003	0.2332 ± 0.0001	1.2077 ± 0.0001
2021-08-04	2430.72423	44.5	8.3		−4.821 ± 0.012	10.73	0.04	10.5992 ± 0.0159	2.0478 ± 0.0002	2.5133 ± 0.0008	0.2267 ± 0.0001	1.1977 ± 0.0004
2021-08-06	2432.65773	88.6	4.3		−4.822 ± 0.006	10.64	0.03	9.8686 ± 0.0051	2.1007 ± 0.0001	2.5649 ± 0.0003	0.2274 ± 0.0001	1.2113 ± 0.0001
2021-08-07	2433.70690	97.3	4.0		−4.748 ± 0.005	10.84	0.06	9.8566 ± 0.0049	2.0708 ± 0.0001	2.5987 ± 0.0003	0.2277 ± 0.0001	1.2163 ± 0.0001
2021-08-16	2442.58811	77.1	5.0		−4.774 ± 0.007	10.67	0.03	11.3262 ± 0.0070	2.3224 ± 0.0001	3.0185 ± 0.0004	0.2538 ± 0.0001	1.2540 ± 0.0002
2021-08-17	2443.55645	118.8	3.3		−4.764 ± 0.004	10.81	0.05	10.8298 ± 0.0038	2.2909 ± 0.0001	2.9997 ± 0.0002	0.2432 ± 0.0001	1.2430 ± 0.0001

Downloaded from https://academic.oup.com/mnras/article/512/4/5067/6552137 by guest on 19 May 2022

Table A1 – *continued*

UT Date	BJD	S/N	σ_{CCF}	Comments	RV	FWHM	BIS	$S_{Ca\,II}$	H α	H β	Na I	He I
–	(BJD$_{TDB}$ – 2 457 000)	–	($\times 10^{-4}$)	–	(km s^{-1})	(km s^{-1})	(km s^{-1})	–	–	–	–	–
2021-08-17	2443.76879	123.7	3.3		−4.822 ± 0.004	10.84	−0.03	10.5793 ± 0.0047	2.2371 ± 0.0001	2.9192 ± 0.0002	0.2419 ± 0.0001	1.2420 ± 0.0001
2021-08-18	2444.57172	127.9	3.0		−5.005 ± 0.004	10.58	0.12	11.0058 ± 0.0034	2.1936 ± 0.0001	2.8456 ± 0.0002	0.2472 ± 0.0001	1.2112 ± 0.0001
2021-08-18	2444.66706	128.1	3.0		−4.956 ± 0.004	10.54	0.06	11.7625 ± 0.0033	2.2827 ± 0.0001	3.0541 ± 0.0002	0.2671 ± 0.0001	1.2569 ± 0.0001
2021-08-18	2444.79139	128.9	3.2		−4.900 ± 0.004	10.57	0.02	11.0667 ± 0.0048	2.2218 ± 0.0001	2.8983 ± 0.0002	0.2518 ± 0.0001	1.2196 ± 0.0001
2021-08-23	2449.53572	87.2	–	Moon	−4.964 ± 0.006	10.53	0.06	11.1271 ± 0.0057	2.3569 ± 0.0001	2.9417 ± 0.0003	0.2337 ± 0.0001	1.2707 ± 0.0001
2021-08-23	2449.65050	64.1	–	Moon	−4.889 ± 0.008	10.57	0.01	10.6075 ± 0.0082	2.2170 ± 0.0002	2.7339 ± 0.0005	0.2301 ± 0.0001	1.2280 ± 0.0002
2021-08-23	2449.78767	44.3	–	Moon	−4.909 ± 0.012	10.67	−0.04	9.4029 ± 0.0153	2.1991 ± 0.0002	2.6674 ± 0.0009	0.2313 ± 0.0001	1.2316 ± 0.0004
2021-09-03	2460.65065	131.4	3.0		−4.556 ± 0.004	10.48	−0.10	9.5292 ± 0.0035	1.9627 ± 0.0001	2.3957 ± 0.0002	0.2178 ± 0.0001	1.1853 ± 0.0001
2021-09-04	2461.56341	113.4	3.4		−4.823 ± 0.005	10.84	0.06	9.8331 ± 0.0036	2.0288 ± 0.0001	2.5706 ± 0.0002	0.2266 ± 0.0001	1.2025 ± 0.0001
2021-09-05	2462.73246	92.7	4.3		−4.717 ± 0.006	10.88	0.05	11.8320 ± 0.0066	2.3776 ± 0.0001	3.1975 ± 0.0003	0.2731 ± 0.0001	1.2613 ± 0.0001
2021-09-06	2463.78569	97.8	4.1		−5.071 ± 0.006	10.69	0.20	10.3435 ± 0.0065	2.1438 ± 0.0001	2.7573 ± 0.0003	0.2428 ± 0.0001	1.2165 ± 0.0001
2021-09-07	2464.53267	106.7	3.7		−4.821 ± 0.005	10.71	−0.01	11.7331 ± 0.0047	2.2921 ± 0.0001	3.0614 ± 0.0003	0.2719 ± 0.0001	1.2176 ± 0.0001
2021-09-10	2467.59928	136.5	2.8		−4.688 ± 0.004	10.89	−0.00	9.6371 ± 0.0024	2.0236 ± 0.0001	2.5127 ± 0.0002	0.2263 ± 0.0001	1.2078 ± 0.0001
2021-09-13	2470.60654	95.3	4.2		−4.464 ± 0.006	10.63	−0.21	9.1327 ± 0.0050	1.9328 ± 0.0001	2.3523 ± 0.0003	0.2144 ± 0.0001	1.1863 ± 0.0001
2021-09-14	2471.55999	135.7	2.9		−4.792 ± 0.004	10.64	0.03	10.8671 ± 0.0030	2.2237 ± 0.0001	2.9136 ± 0.0002	0.2547 ± 0.0001	1.2740 ± 0.0001
2021-09-15	2472.57476	117.1	–	Flare	−4.785 ± 0.005	10.82	0.03	10.8393 ± 0.0031	2.6923 ± 0.0001	3.4396 ± 0.0002	0.3142 ± 0.0001	1.3673 ± 0.0001
2021-09-18	2476.49416	108.9	3.6		−4.839 ± 0.005	10.63	0.05	10.0083 ± 0.0039	2.1494 ± 0.0001	2.6948 ± 0.0002	0.2362 ± 0.0001	1.2195 ± 0.0001
2021-09-20	2477.52519	70.9	5.4		−4.753 ± 0.008	10.89	−0.01	9.7041 ± 0.0072	2.0953 ± 0.0001	2.6260 ± 0.0005	0.2308 ± 0.0001	1.2084 ± 0.0002
2021-09-20	2477.63321	62.0	6.3		−4.802 ± 0.009	10.92	−0.01	9.2273 ± 0.0092	2.0483 ± 0.0002	2.5155 ± 0.0006	0.2239 ± 0.0001	1.1899 ± 0.0002
2021-09-20	2478.50883	96.4	4.0		−5.040 ± 0.005	10.59	0.17	10.4409 ± 0.0045	2.1095 ± 0.0001	2.6825 ± 0.0003	0.2380 ± 0.0001	1.2080 ± 0.0001
2021-09-21	2478.65930	110.9	3.6		−4.976 ± 0.005	10.57	0.10	11.0016 ± 0.0049	2.1774 ± 0.0001	2.8682 ± 0.0003	0.2571 ± 0.0001	1.2491 ± 0.0001
2021-09-22	2479.51606	54.5	6.8		−4.759 ± 0.009	10.71	0.06	9.9181 ± 0.0090	2.0058 ± 0.0002	2.4825 ± 0.0006	0.2270 ± 0.0001	1.2233 ± 0.0003
2021-09-22	2479.71843	85.8	4.7		−4.770 ± 0.006	10.53	0.08	10.3132 ± 0.0072	2.1107 ± 0.0001	2.7327 ± 0.0004	0.2404 ± 0.0001	1.2201 ± 0.0001

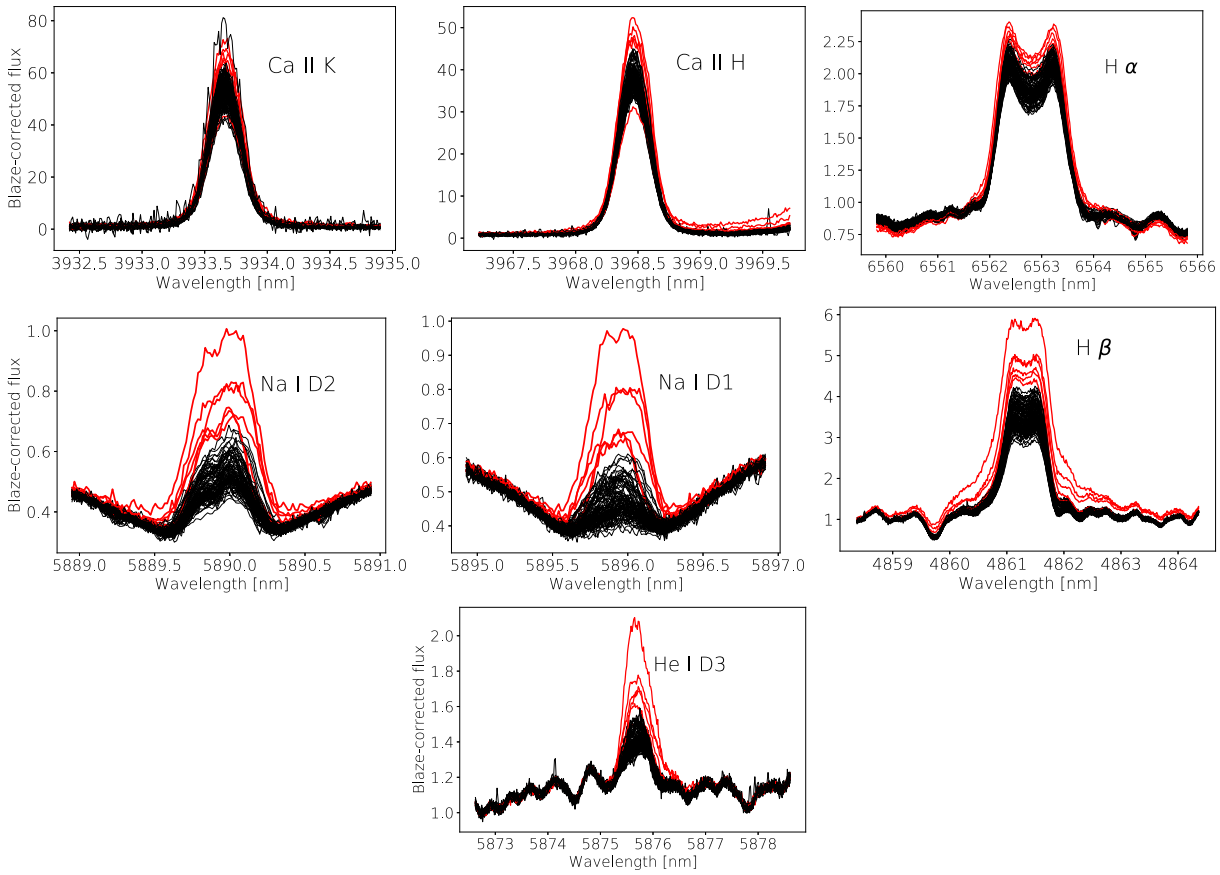


Figure B1. Observed emission reversals of Ca II H & K, H α, Na I D1 & D2, H β, and He I D3 chromospheric lines for AU Mic. In each panel, profiles shown in red were flagged as affected by a stellar flare (six observations). Note that the Moon-polluted observations (2021-08-23) are not included in these plots.

B2 Correlation analysis

Each pair of activity indicator computed for this study (i.e. RV, FWHM, BIS, and chromospheric emission indices based on Ca II H & K, H α, H β, Na I D1 & D2, and He I D3 lines) is plotted in Fig. B2, whereas the associated Pearson correlation coefficient are given in Table B1.

B3 Periodograms

The Bidimensional periodograms the chromospheric emission lines except He I (shown in Fig. 3) are shown in Fig. B3 (including the observations affected by stellar flares in the input data set) and Fig. B4 (excluding the observations affected by stellar flares from the input data set).

Downloaded from https://academic.oup.com/mnras/article/512/4/5067/6552137 by guest on 19 May 2022

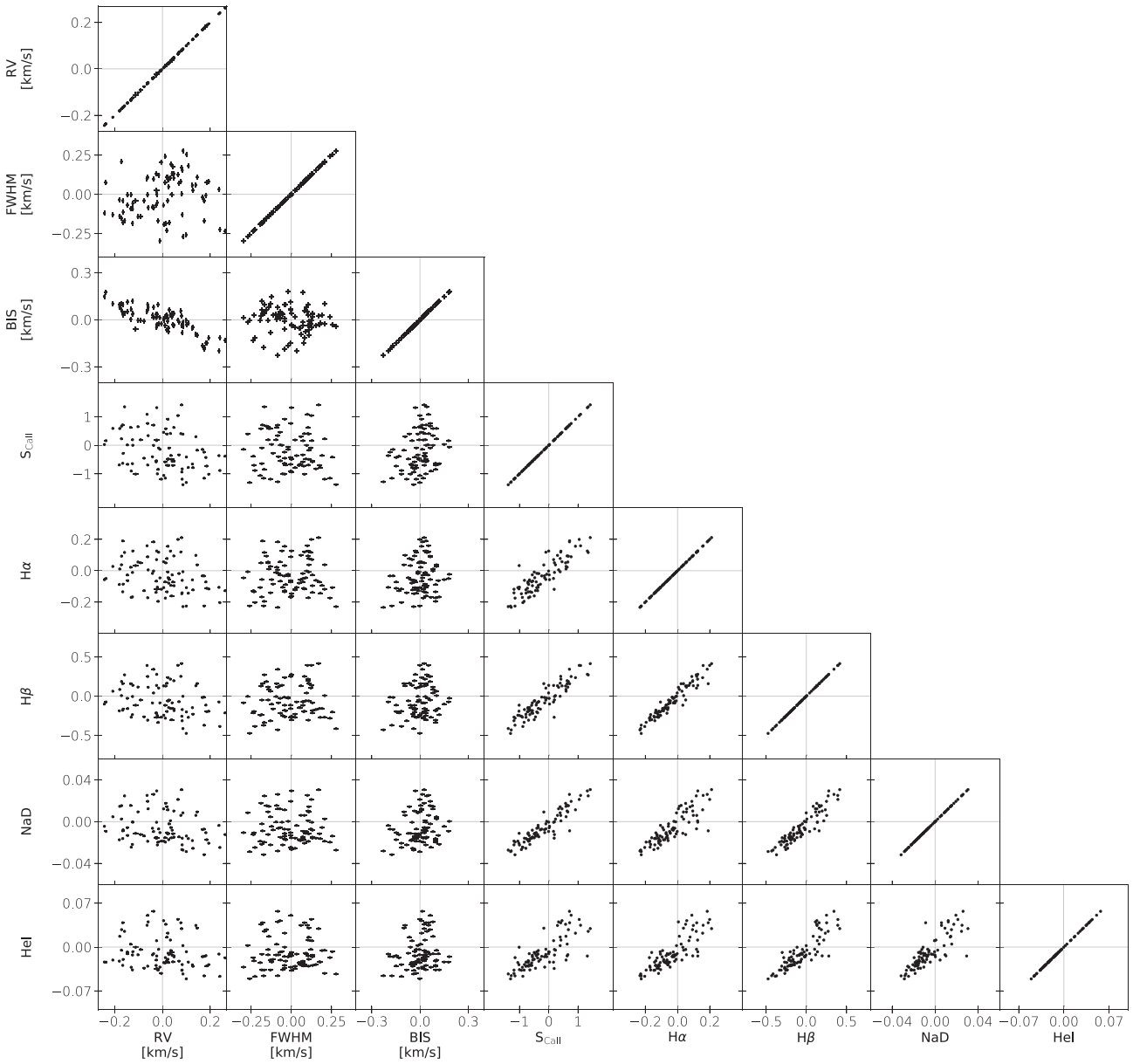


Figure B2. Correlation plots of the activity indicators analysed in Section 3. The person correlation coefficients between each pair of time-series are listed in Table B1.

Downloaded from https://academic.oup.com/mnras/article/512/4/5067/6552137 by guest on 19 May 2022

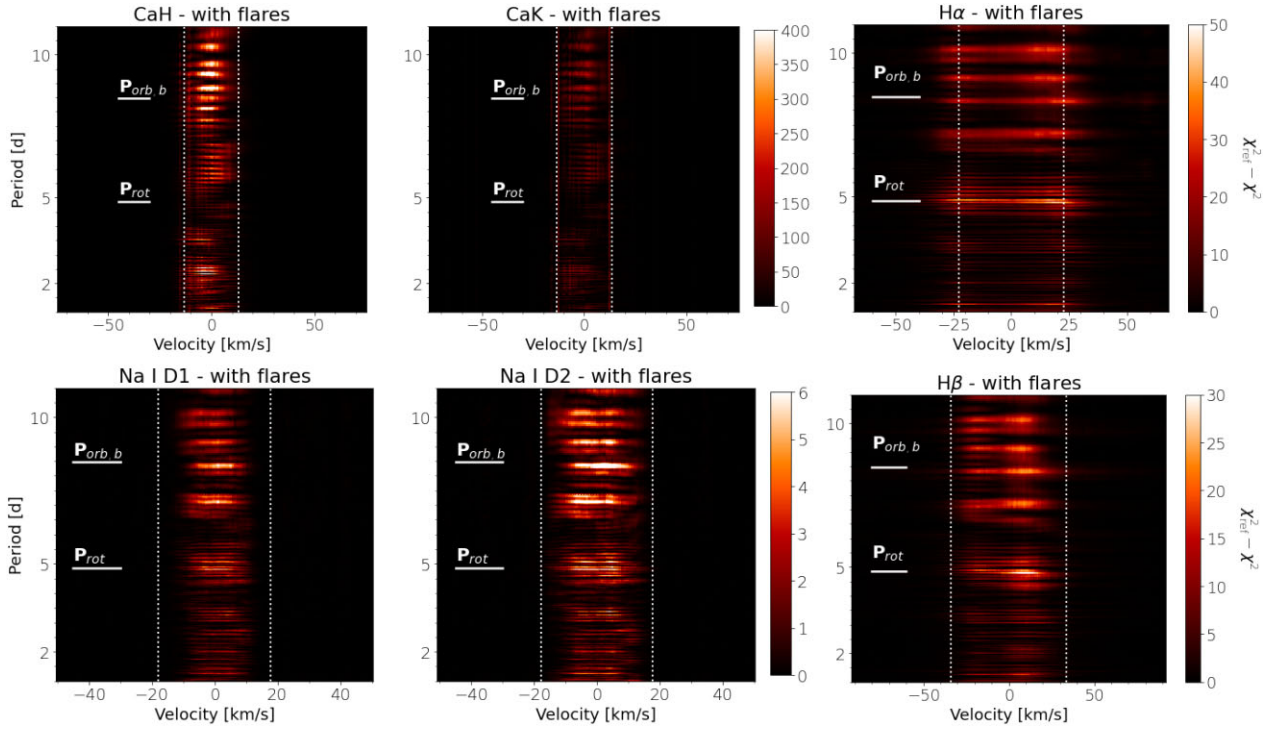


Figure B3. Bidimensional periodograms of the Ca II H & K, H α, Na I D1 & D2 and H β chromospheric lines, when all observations, including the ones affected by stellar flares, are included in the input data set. As in Fig. 3, the two vertical lines delimit the line width and we indicate the orbital period of AU Mic b, $P_{\rm orb,\,b}$, and the rotation period of the star, $P_{\rm rot}$, by the two horizontal lines. The colour map depicts the power of the periodogram normalized to the most powerful peak.

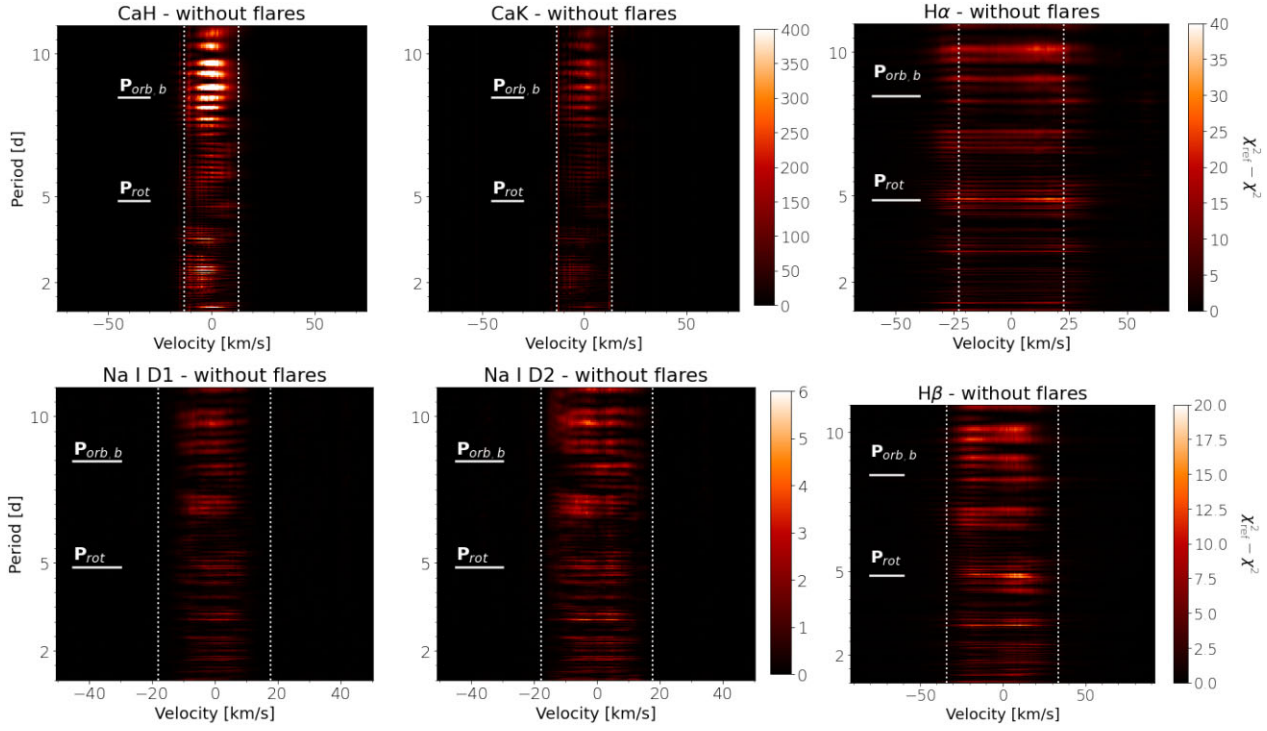


Figure B4. Same a Fig. B3, except that, this time, the observations affected by flares were excluded from the input data set beforehand.

Downloaded from https://academic.oup.com/mnras/article/512/4/5067/6552137 by guest on 19 May 2022

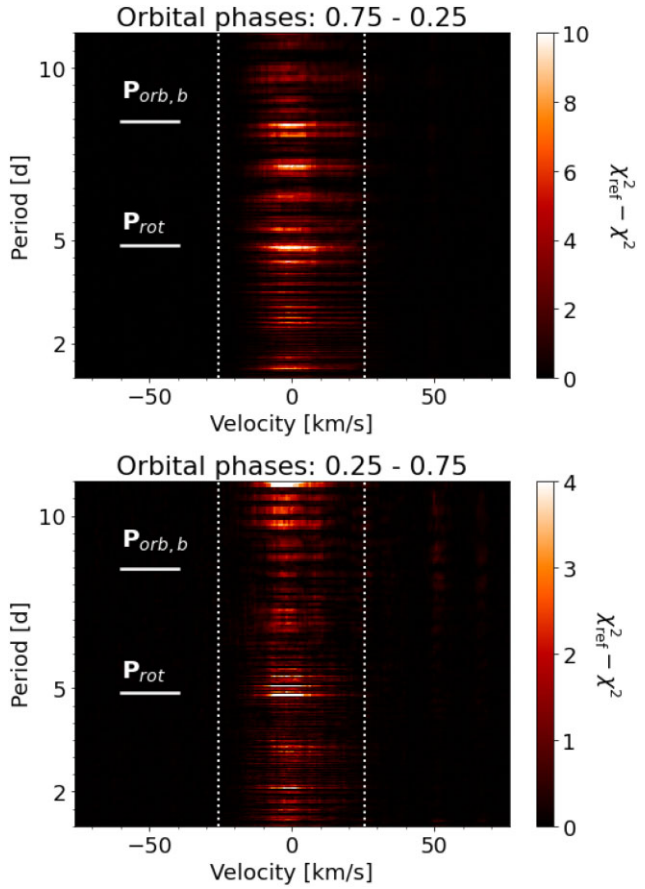


Figure B5. Bidimensional periodograms of the He I line obtained by only keeping the observations where AU Mic b is (i) closer from the observer than the star (orbital phase between 0.75 and 0.25; *top panel*), and (ii) further from the observer than the star (orbital phase between 0.25 and 0.75; *bottom panel*.

Table B1. Pearson correlation coefficients between the different time-series of activity indicators after removing the epochs affected by flares.

	RV	FWHM	BIS	S_{CaII}	H α	H β	Na I
FWHM	0.124	–	–	–	–	–	–
BIS	− 0.861	− 0.062	–	–	–	–	–
S_{CaII}	− 0.336	− 0.066	0.263	–	–	–	–
Hα	− 0.245	0.101	0.169	0.846	–	–	–
Hβ	− 0.258	0.064	0.180	0.922	0.946	–	–
Na	− 0.297	− 0.051	0.226	0.906	0.892	0.904	–
He I	− 0.145	0.036	0.148	0.751	0.785	0.837	0.808

This paper has been typeset from a TEX/LATEX file prepared by the author.

Downloaded from https://academic.oup.com/mnras/article/512/4/5067/6552137 by guest on 19 May 2022